

# Detecting permafrost active layer thickness change from nonlinear baseflow recession

Matthew G Cooper<sup>1</sup>, Tian Zhou<sup>1</sup>, Katrina E. Bennett<sup>2</sup>, Robert Bolton<sup>3</sup>, Ethan Coon<sup>4</sup>, Sean W Fleming<sup>5</sup>, Joel Carey Rowland<sup>6</sup>, and Jon Schwenk<sup>7</sup>

<sup>1</sup>Pacific Northwest National Laboratory

<sup>2</sup>Los Alamos National Lab

<sup>3</sup>IARC

<sup>4</sup>Oak Ridge National Laboratory

<sup>5</sup>USDA

<sup>6</sup>Los Alamos National Laboratory (DOE)

<sup>7</sup>Los Alamos National Laboratory

November 21, 2022

## Abstract

Permafrost underlies approximately one fifth of the global land area and affects ground stability, freshwater runoff, soil chemistry, and surface-atmosphere gas exchange. The depth of thawed ground overlying permafrost (active layer thickness, *ALT*) has broadly increased across the Arctic in recent decades, coincident with a period of increased streamflow, especially the lowest flows (baseflow). Mechanistic links between *ALT* and baseflow have recently been explored using linear reservoir theory, but most watersheds behave as nonlinear reservoirs. We derive theoretical nonlinear relationships between long-term average saturated soil thickness  $\eta$  (proxy for *ALT*) and long-term average baseflow. The theory is applied to 38 years of daily streamflow data for the Kuparuk River basin on the North Slope of Alaska. Between 1983–2020, the theory predicts that  $\eta$  increased  $0.11 \pm 0.17 [2\sigma]$   $\mu\text{m a}^{-1}$ , or  $4.4 \pm 6.6$  cm total. The rate of change nearly doubled to  $0.20 \pm 0.24$  cm  $\text{a}^{-1}$  between 1990–2020, during which time field measurements from CALM (Circumpolar Active Layer Monitoring) sites in the Kuparuk indicate  $\eta$  increased  $0.31 \pm 0.22$  cm  $\text{a}^{-1}$ . The predicted rate of change more than doubled again between 2002–2020, mirroring a near doubling of observed *ALT* rate of change. The inferred increase in  $\eta$  is corroborated by GRACE (Gravity Recovery and Climate Experiment) satellite gravimetry, which indicates that terrestrial water storage increased  $\sim 0.80 \pm 3.40$  cm  $\text{a}^{-1}$ ,  $\sim 56\%$  higher than the predicted increase in  $\eta$ . Overall, hydrologic change is accelerating in the Kuparuk River basin, and we provide a theoretical framework for estimating changes in active layer water storage from streamflow measurements alone.

1  
2 **Detecting permafrost active layer thickness change from nonlinear baseflow**  
3 **recession**

4 **M.G. Cooper<sup>1</sup>, T. Zhou<sup>1</sup>, K.E. Bennett<sup>2</sup>, W.R. Bolton<sup>3</sup>, E.T. Coon<sup>4</sup>, S.W. Fleming<sup>5,6,7</sup>, J.C.**  
5 **Rowland<sup>2</sup>, and J. Schwenk<sup>2</sup>**

6 <sup>1</sup>Atmospheric Sciences and Global Change Division, Pacific Northwest National Laboratory,  
7 Richland, WA, USA.

8 <sup>2</sup>Earth and Environmental Sciences Division, Los Alamos National Laboratory, Los Alamos,  
9 NM, USA.

10 <sup>3</sup>International Arctic Research Center, University of Alaska Fairbanks, Fairbanks, AK, USA.

11 <sup>4</sup>Climate Change Science Institute and Environmental Sciences Division, Oak Ridge National  
12 Laboratory, Oak Ridge, TN, USA.

13 <sup>5</sup>National Water and Climate Center, Natural Resources Conservation Service, US Department  
14 of Agriculture, Portland OR, USA.

15 <sup>6</sup>College of Earth, Ocean, and Atmospheric Sciences, and Water Resources Graduate Program,  
16 Oregon State University, Corvallis, OR, USA.

17 <sup>7</sup>Department of Earth, Ocean, and Atmospheric Science, University of British Columbia, BC,  
18 Canada.

19  
20 Corresponding author: Matthew Cooper ([matt.cooper@pnnl.gov](mailto:matt.cooper@pnnl.gov))

21 **Key Points:**

- 22 • New relationships between active layer thickness and baseflow are developed for  
23 application to catchments underlain by permafrost.
- 24 • Theoretical predictions of active layer thickness trends agree with measured trends on the  
25 North Slope of Arctic Alaska.
- 26 • Novel methods are developed to estimate nonlinear recession flow parameters and related  
27 hydrologic signatures using generalized Pareto distributions.

28 **Abstract**

29 Permafrost underlies approximately one fifth of the global land area and affects ground stability,  
30 freshwater runoff, soil chemistry, and surface-atmosphere gas exchange. The depth of thawed  
31 ground overlying permafrost (active layer thickness, *ALT*) has broadly increased across the  
32 Arctic in recent decades, coincident with a period of increased streamflow, especially the lowest  
33 flows (baseflow). Mechanistic links between *ALT* and baseflow have recently been explored  
34 using linear reservoir theory, but most watersheds behave as nonlinear reservoirs. We derive  
35 theoretical nonlinear relationships between long-term average saturated soil thickness  $\bar{\eta}$  (proxy  
36 for *ALT*) and long-term average baseflow. The theory is applied to 38 years of daily streamflow  
37 data for the Kuparuk River basin on the North Slope of Alaska. Between 1983–2020, the theory  
38 predicts  $\bar{\eta}$  increased  $0.11 \pm 0.17 [2\sigma]$  cm a<sup>-1</sup>, or  $4.4 \pm 6.6$  cm total. The rate of change nearly  
39 doubled to  $0.20 \pm 0.24$  cm a<sup>-1</sup> between 1990–2020, during which time field measurements from  
40 CALM (Circumpolar Active Layer Monitoring) sites in the Kuparuk indicate *ALT* increased  
41  $0.31 \pm 0.22$  cm a<sup>-1</sup>. The predicted rate of change more than doubled again between 2002–2020,  
42 mirroring a near doubling of observed *ALT* rate of change. The inferred increase in  $\bar{\eta}$  is  
43 corroborated by GRACE (Gravity Recovery and Climate Experiment) satellite gravimetry,  
44 which indicates that terrestrial water storage increased  $\sim 0.80 \pm 3.40$  cm a<sup>-1</sup>,  $\sim 56\%$  higher than  
45 the predicted increase in  $\bar{\eta}$ . Overall, hydrologic change is accelerating in the Kuparuk River  
46 basin, and we provide a theoretical framework for estimating changes in active layer water  
47 storage from streamflow measurements alone.

48

49 **Plain Language Summary**

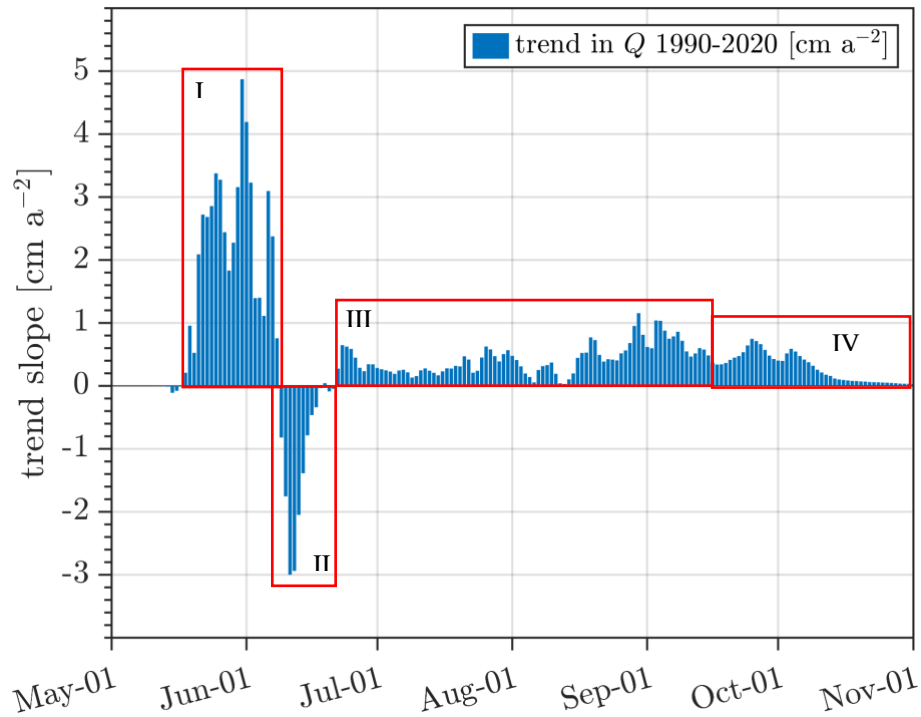
50 Streamflow has increased in most areas of the Arctic in recent decades. This increase in  
51 streamflow has occurred along with a period of rising air temperatures and thawing permafrost.  
52 Permafrost is typically overlain by a layer of seasonally unfrozen ground referred to as the active  
53 layer, which gets deeper as permafrost thaws. As the active layer deepens, it can store more  
54 water. Water may also take more time to flow through a thicker active layer than it would atop  
55 frozen ground. Because there is more space to store water, thicker active layers leads to  
56 increased soil water storage which sustains streamflow during dry periods and enhances overall  
57 increased streamflow and subsurface flow. We developed an approach to measure how quickly  
58 the active layer thickness is changing using the rate of change of streamflow. This is useful  
59 because streamflow measurements are widely available and easy to obtain, whereas active layer  
60 thickness measurements are difficult to measure and therefore uncommon. If the equations we  
61 developed accurately predict measured values, the pace at which active layer thickness changes  
62 can be estimated from streamflow measurements, which would expand the current knowledge of  
63 permafrost thaw rates and provide an independent way to validate simulations of active layer  
64 thickness.

65

## 66 **1 Introduction**

67 Permafrost underlies approximately one fifth of the global land area and is an important  
68 control on slope stability, shoreline erosion, water available for runoff, soil biogeochemistry, and  
69 gas exchange between the land surface and atmosphere (McKenzie et al., 2021; Walvoord &  
70 Kurylyk, 2016). The layer of seasonally-thawed ground overlying permafrost known as active  
71 layer is a sensitive indicator of permafrost response to climate change (Kurylyk et al., 2014). In  
72 recent decades, active layer thickness (*ALT*) has increased at high latitude observation sites,  
73 concurrent with observed increases in streamflow, especially the lowest flows (hereafter referred  
74 to as *baseflow*) (Duan et al., 2017; Rennermalm et al., 2010; Smith et al., 2007).

75 The trends in *ALT* and baseflow are thought to be linked via: 1) increased soil water  
76 storage capacity within a thicker active layer, 2) increased soil water residence time as flow paths  
77 lengthen within a more continuous active layer, and 3) direct contribution of thaw water to  
78 streamflow, each of which may support higher baseflow in high latitude rivers (Figure 1)  
79 (Brutsaert & Hiyama, 2012; Evans et al., 2020; Jacques & Sauchyn, 2009; Lyon & Destouni,  
80 2010; Walvoord et al., 2012; Walvoord & Striegl, 2007). In addition, heat transport via lateral  
81 subsurface flow within the active layer enhances permafrost thaw (Rowland et al., 2011; Sjöberg  
82 et al., 2021), suggesting a positive feedback. Changes in the water balance driven by  
83 precipitation and evaporation are also thought to have contributed to a broad-scale increase in  
84 freshwater runoff delivered to the Arctic Ocean in recent decades (Feng et al., 2021).



85

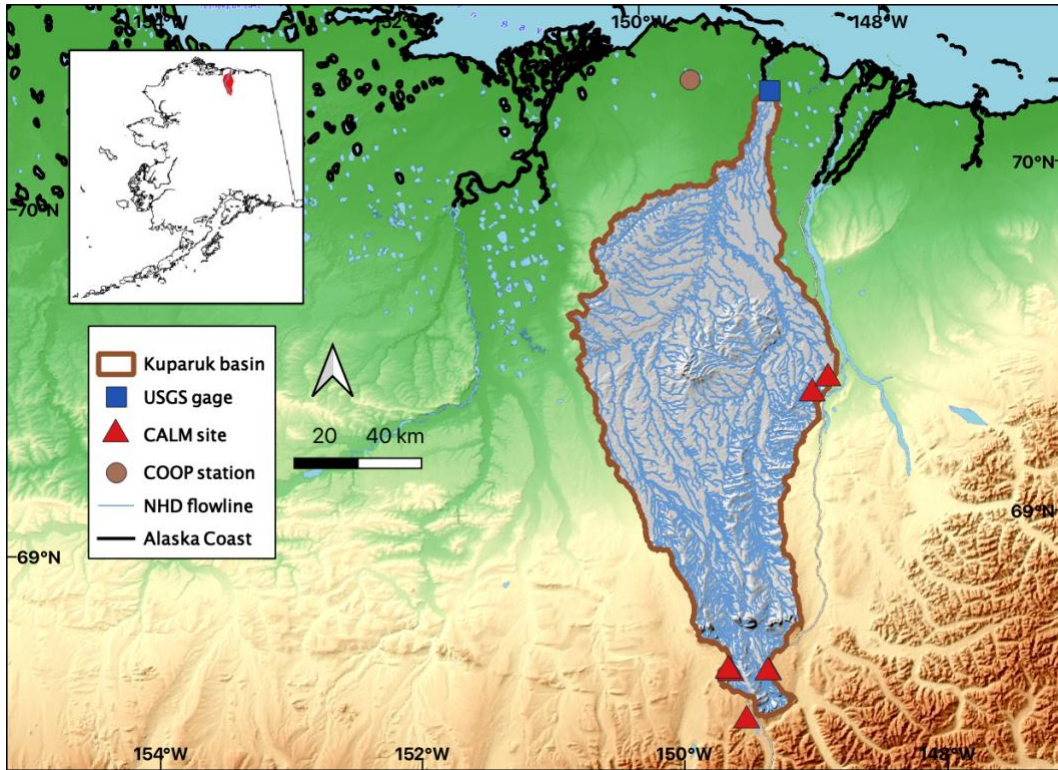
86

87 **Figure 1:** Trend in daily streamflow for each day from 15 May to 1 December for the Kuparuk River on  
 88 the North Slope of Arctic Alaska. Four conceptual periods are highlighted by red box with hypothetical  
 89 explanations: I) higher May–June flows driven by earlier snowmelt, II) lower June flows driven by  
 90 snowmelt deficit, III) higher June–September flows driven by increased precipitation, and IV) higher  
 91 September–December flows driven by increased baseflow. The approximately smooth increase followed  
 92 by smooth recession of the daily trend magnitudes during period IV supports the idea that permafrost  
 93 thaw and increased catchment storage are supplying additional water to baseflow, rather than a process  
 94 such as precipitation that might resemble the quasi-random structure of period III. River discharge data  
 95 are provided by United States Geological Survey (gage 1596000).

96 One approach to analyzing mechanistic links between *ALT* change and streamflow  
 97 change is baseflow recession analysis (Brutsaert & Hiyama, 2012; Evans et al., 2020), which is a  
 98 classical method in hydrology that relates groundwater storage  $S$  to recession flow  $Q$  with a  
 99 power function relationship:  $Q = c(S - S_c)^{1/\beta}$ , where  $S_c$  is a critical storage below which the  
 100 relationship does not hold,  $c$  is a scale parameter related to aquifer properties via hydraulic  
 101 groundwater theory, and  $\beta$  is an order parameter indicating the degree of nonlinearity in the  
 102 storage-discharge relationship. For the special case of a linear reservoir ( $\beta = 1$ ), simple  
 103 relationships between long-term change in *ALT* and long-term change in  $Q$  can be derived under  
 104 the assumption that  $S$  is primarily a function of water storage in active layer, that is, the saturated  
 105 *ALT* (Brutsaert & Hiyama, 2012).

106           If these simple relationships are applicable to real-world catchments, it suggests *ALT*  
107 trends can be diagnosed from streamflow measurements alone. However, streamflow recession  
108 in real-world catchments is typically not consistent with linear reservoir theory, meaning  
109 real-world recession data suggest  $\beta \neq 1$  (Aksoy & Wittenberg, 2011; Jachens et al., 2020).  
110 Although nonlinear reservoir behavior is well-documented and widely explored in the hydrologic  
111 science literature, to our knowledge, the theoretical relationship between saturated *ALT* change  
112 and baseflow has not been generalized to the nonlinear case (Hinzman et al., 2020; Sergeant et  
113 al., 2021). Doing so could open the door to retrospective analysis of *ALT* change at broad scales  
114 and is necessary before such methods can be applied beyond the special case of linear reservoir  
115 theory. Exploring the nonlinear case also merits attention because the parameter  $\beta$  can be related  
116 to aquifer properties (Rupp & Selker, 2006b), which adds another dimension along which *ALT*  
117 can be related to streamflow, which is more widely observed than *ALT*.

118           The aim of this paper is to generalize the hydraulic groundwater theory of streamflow  
119 sensitivity to saturated *ALT* change to the case of nonlinear storage-discharge behavior. Section 2  
120 describes the background to the theory. In Section 3, we extend an earlier theory (Brutsaert &  
121 Hiyama, 2012) of saturated *ALT* change for flat catchments with homogeneous soils and linear  
122 storage-discharge behavior to the case of sloped catchments with non-homogeneous soils and  
123 nonlinear storage-discharge behavior. The non-homogeneity considered here is vertical variation  
124 in saturated lateral hydraulic conductivity (Rupp & Selker, 2006b). These three characteristics  
125 are consistent with real-world catchment behavior, although we emphasize the theory remains an  
126 effective one based on hillslope-scale behavior. The main theoretical result is a set of new  
127 equations (Section 3) that relate long-term average saturated *ALT* change to long-term baseflow  
128 change. In Section 4 we describe a baseflow recession algorithm that implements the theory and  
129 in Section 5 we apply it to 38 years of daily streamflow and 30 years of annual *ALT* measured in  
130 the Kuparuk River basin on the North Slope of Alaska (Figure 2). Section 6 compares  
131 predictions to observations. The paper concludes with a discussion of methodological  
132 limitations, which include high sensitivity to accurate knowledge of soil properties, and the  
133 dependence on large-sample streamflow data to estimate power-law scaling of recession flows.



134

135 **Figure 2:** Study area map showing Kugaruk basin outline, locations of United States Geological Survey  
 136 (USGS) gage 1596000, Circumpolar Active Layer Monitoring network sites, and United States National  
 137 Oceanic and Atmospheric Administration Cooperative Observer Program weather station 505136.  
 138 Kugaruk basin topography is from USGS interferometric synthetic aperture radar 5 m resolution digital  
 139 terrain model. Basemap credit: ©OpenTopoMap (CC-BY-SA).

## 140 2 Hydraulic groundwater theory

### 141 2.1 Storage-discharge relationship

142 Baseflow recession analysis relates groundwater storage  $S$  to baseflow  $Q$  with a  
 143 single-valued catchment-scale storage-discharge relationship:

$$144 \quad Q = c(S - S_c)^{1/\beta}, \quad \beta \neq 0 \quad (1)$$

145 where baseflow  $Q$  has dimensions  $L/T$ , scale parameter  $c$  has dimensions  $L^{(b-1)/(b-2)}/T$ , order  
 146 parameter  $\beta$  is dimensionless, and  $S_c = S(Q \rightarrow Q_{\min})$  is a critical storage below which (1) does  
 147 not hold.

148 During periods when precipitation, evaporation, and any other factor that affects  
 149 catchment water storage is negligible relative to streamflow, the rate of change of catchment  
 150 water storage can be approximated by the conservation equation:

$$151 \quad \frac{dS}{dt} = -Q, \quad (P - E \cong 0) \quad (2)$$

152 where  $S$  has dimension  $L$  and represents water stored in upstream catchment aquifers available to  
 153 supply  $Q$ . With (1) and (2), the rate of change of  $Q$  can be expressed as a power function of  $Q$ :

$$154 \quad -\frac{dQ}{dt} = aQ^b \quad (3)$$

155 where parameter  $a$  has dimensions  $T^{(b-2)}/L^{(b-1)}$ ,  $b$  is dimensionless, and the parameters in (1) and  
 156 (3) are related as  $c = (a\beta)^{1/\beta}$  and  $\beta = 2 - b$ .

157 At hillslope scales, (1) and (3) acquire physical meaning from solutions to the  
 158 one-dimensional (1-D) lateral groundwater flow equation:

$$159 \quad \frac{\partial h}{\partial t} = \frac{k_D}{\phi} \frac{D^{-n}}{(n+1)} \frac{\partial}{\partial x} \left[ h^{n+1} \left( \frac{\partial h}{\partial x} \cos \theta + \sin \theta \right) \right] + \frac{I}{\phi} \quad (4)$$

160 where  $h(x, t)$  is the phreatic water surface along horizontal dimension  $x$ ,  $\phi$  is drainable porosity,  
 161  $D$  is aquifer thickness,  $n$  is a constant,  $\theta$  is bed slope,  $I$  is recharge rate, and:

$$162 \quad k(z) = k_D (z/D)^n, \quad (5)$$

163 is lateral saturated hydraulic conductivity along vertical dimension  $z$  with  $k_D = k(D)$ . Various  
 164 approximate and exact solutions to (4) for an unconfined aquifer draining to a fully- or  
 165 partially-penetrating channel can be written in the same form as (3) (Appendix A) (Brutsaert &  
 166 Nieber, 1977; van de Giesen et al., 2005; Rupp & Selker, 2006b). At catchment scales,  $a$  and  $b$   
 167 can be interpreted as lumped parameters linked to catchment-effective drainage density and  
 168 aquifer transmissivity, porosity, slope, and breadth (distance along the land surface from channel  
 169 to catchment divide) (Brutsaert, 2005). In the linear case ( $b = 1 \leftrightarrow n = 0$ ), the solution to (3) is  
 170 an exponential  $Q \sim e^{-at}$  with decay constant  $a$  (Boussinesq, 1903). For  $b > 1$ , the solution to (3)  
 171 is a power function  $Q \sim t^{-\alpha}$  with  $\alpha = 1/(b - 1)$  (Section 2.3).

## 172 **2.2 Drainable porosity and the effective water table**

173 The groundwater stored in a catchment can be defined in terms of a thickness of liquid  
 174 water stored in an effective catchment aquifer (Brutsaert & Hiyama, 2012):

$$175 \quad (S - S_r) = \phi \eta \quad (6)$$

176 where  $\eta$  is an effective water table thickness [ $L$ ] relative to an arbitrary reference  $S_r$ . In this  
 177 study, we assume  $S_c = S_r$ . In general,  $S_c \neq 0$  but it's absolute magnitude has no bearing on the  
 178 following analysis (Kirchner, 2009).

179 In this study and in the general context of hydraulic groundwater theory, the active  
 180 groundwater layer is treated as a Boussinesq aquifer. Under the Dupuit-Forchheimer assumption  
 181 for an unconfined aquifer, vertical fluxes are assumed negligible relative to horizontal fluxes and  
 182 the water table is treated as a free surface, implying capillarity is also neglected (Brutsaert,  
 183 2005). The effect of capillarity on storage change can be parameterized in terms of  $\phi$ , defined as  
 184 the change in storage per unit area per unit change in effective water table (Brutsaert, 2005):

$$185 \quad \phi = \frac{\partial S}{\partial \eta} = \frac{1}{d\eta/dD} \frac{\partial S}{\partial D}, \quad 0 < \phi < 1, \quad (7)$$

186 where  $\eta$  is a quasi-steady (“average”) groundwater layer thickness. Equation (7) extends the  
 187 usual form  $\phi = \partial S / \partial \eta$  to a timescale over which  $D$  is changing and assumes  $d\eta/dD$  is a linear  
 188 function of  $D$  over the timescale and soil thickness represented by  $(d\eta/dD)\Delta D$ . It does not  
 189 assume a functional form for  $\phi$  during recession, but such assumptions are made in Section 4.

### 190 **2.3 Characteristic timescales**

191 With (2) and (3), a storage sensitivity function can be defined:

$$192 \quad \frac{dS}{dQ} = \tau(Q), \quad (8)$$

193 where:

$$194 \quad \tau(Q) = a^{-1} Q^{1-b} \quad (9)$$

195 is a nonlinear drainage timescale that carries the dimension of  $dt$  in (3). Note that  $\tau^{-1}(Q) =$   
 196  $dQ/dS$  is denoted  $g(Q)$  elsewhere (Berghuijs et al., 2016; Kirchner, 2009).

197 Integration of (3) over some time interval  $t - t_0$ , with  $t_0 = 0$  gives:

$$198 \quad Q(t) = [Q_0^{1-b} + a(b-1)t]^{\frac{1}{1-b}} \quad (10)$$

199 and integration of (8) gives a mathematically identical form parameterized by  $S(t)$ :

$$200 \quad Q(t) = [a(2-b)(S - S_r)]^{\frac{1}{2-b}} \quad (11)$$

201 thereby recovering (1).

202 Although  $\tau$  has dimension time, (9) implies non-characteristic time scaling, since  $\tau$  is a  
 203 function of  $Q$ . However, we can estimate an expected value  $\langle \tau \rangle$  from the probability density  
 204 transform of (10). Evaluating  $\int_{Q_0}^0 d\tau C \cdot Q(\tau) = 1$ , where  $Q(\tau) = Q_0(\tau/\tau_0)^{1/(1-b)}$  and  $C$   
 205 normalizes the integral if  $1 < b < 2$ , we find:

$$206 \quad p(\tau) = \left(\frac{2-b}{b-1}\right) \left(\frac{1}{\tau_0}\right) \left(1 + \frac{\tau - \tau_0}{\tau_0}\right)^{\frac{1}{1-b}}, \quad \tau_0 \leq \tau \text{ and } 1 < b < 2 \quad (12)$$

207 which is a generalized Pareto (GP) distribution with shape parameter  $\zeta = (b-1)/(2-b)$ , scale  
 208 parameter  $\sigma = \tau_0(b-1)/(2-b)$ , and threshold parameter  $\mu = \tau_0$ . In this case  $\mu = \sigma/\zeta$  and  
 209 therefore (10) is equivalent to an unbounded Pareto distribution:  $p(\tau) = (\alpha-1)/\tau_0(\tau/\tau_0)^{-\alpha}$ ,  
 210 with shape parameter  $\alpha = 1/(b-1)$  and scale parameter  $\tau_0$ .

211 A general feature of a power law such as (12) is that the process it describes lacks a  
 212 characteristic timescale for  $1 < b$ . Moreover, if  $3/2 \leq b$ ,  $\langle \tau \rangle \rightarrow +\infty$  for  $0 < Q_0$ , where  $\langle \tau \rangle =$   
 213  $\int d\tau \tau \cdot p(\tau)$ . For  $1 < b \leq 3/2$ , however:

$$214 \quad \langle \tau \rangle = \tau_0 \left(\frac{2-b}{3-2b}\right), \quad \langle Q \rangle = Q_0 \left(\frac{2-b}{3-b}\right), \quad \langle t \rangle = \tau_0 \left(\frac{1}{3-2b}\right) \quad (13)$$

215 where  $\langle \tau \rangle$  is an expected drainage timescale,  $\langle Q \rangle$  is an expected value of baseflow, and  $\langle t \rangle$  is an  
 216 expected duration of baseflow. Note  $\langle Q \rangle$  remains finite for  $1 < b < 2$ .

217 As implied by (12), a critical threshold exists at  $b = 2$ , above which (10) is not  
 218 normalizable. In the context of (4),  $b = 2$  marks a transition from small- $t$  (“early-time”) to  
 219 large- $t$  (“late-time”) drainage, where theoretical and numerical solutions indicate  $b = 3$  (but can  
 220 approach  $+\infty$ ) during early-time and  $1 < b < 2$  during late-time, separated by an “intermediate”  
 221 period (van de Giesen et al., 2005; Rupp & Selker, 2006b).

222 In general, (11) will be used to derive expressions relating  $ALT$  to baseflow, with (12)  
 223 and (13) providing a method to estimate  $\langle \tau \rangle$  and  $\langle Q \rangle$ , and the basis for a discussion of the  
 224 important dependence on  $\tau_0$ .

225 **3 New equations for change in permafrost active groundwater layer thickness from**  
 226 **nonlinear baseflow recession analysis**

227 We first rewrite (11) with  $a$  and  $S$  parameterized by  $D$  (dependence on time is omitted for  
 228 clarity):

$$229 \quad \bar{Q} = [a(D)(2 - b)(\overline{S(D)} - S_r)]^{\frac{1}{2-b}} \quad (14)$$

230 where overbars indicate temporal averages over a period comparable to  $\langle t \rangle$ . The total derivative  
 231 of (14) in this case is:

$$232 \quad \frac{d\bar{Q}}{dt} = \frac{\partial \bar{Q}}{\partial t} + \left( \frac{\partial \bar{Q}}{\partial S} \frac{\partial \overline{S}}{\partial D} + \frac{\partial \bar{Q}}{\partial a} \frac{\partial a}{\partial D} \right) \frac{dD}{dt} \quad (15)$$

233 where  $\partial S / \partial D$  is defined in (7). Strictly speaking,  $D$  represents the initial saturated aquifer  
 234 thickness when  $Q = Q_0$ , and  $\eta$  is the average saturated aquifer thickness over a period  
 235 comparable to  $\langle t \rangle$ . As in prior studies (Brutsaert & Hiyama, 2012; Lyon et al., 2009),  $D$  is treated  
 236 as proxy for  $ALT$  and  $\bar{\eta}$  as proxy for its average value, and hereafter we use them  
 237 interchangeably in the context of (15).

238 Given (6), (9) and (14), (15) can be written:

$$239 \quad \frac{d\bar{Q}}{dt} = \frac{\partial \bar{Q}}{\partial t} + \frac{\phi}{\tau} \left( 1 + \frac{D}{a} \frac{\partial a}{\partial D} \right) \frac{d\bar{\eta}}{dt}. \quad (16)$$

240 A general result of hydraulic groundwater theory is that  $a$  can be expressed as a power  
 241 function of  $D$ :  $a \propto D^N$ , where  $N$  is a constant function of  $b$  and can be related to  $k(z)$  (Appendix  
 242 A). For the present case, we reviewed 19 different solutions to (4) collated in Figure 2 and Figure  
 243 3 of Rupp and Selker (2006b) (hereafter RS06). Setting aside two kinematic-wave solutions  
 244 (Beven, 1982), we found for the 17 remaining solutions  $a$  can be written as:

$$245 \quad a(D) = c_1 D^N (1 + c_2 D^M) \quad (17)$$

246 where  $c_1$  and  $c_2$  are constants that depend on the particular solution. For all six  
 247 horizontal-aquifer solutions and six sloped-aquifer solutions,  $c_2 = 0$ . Five sloped-aquifer  
 248 solutions having  $c_2 \neq 0$  effectively treat  $a(D)$  as the horizontal equivalent multiplied by a  
 249 dimensionless slope factor  $\nu = B/D \tan \theta$ . In these cases, if  $\nu$  is treated as a constant parameter,  
 250  $c_2 D^M$  is constant, and (17) satisfies the following general property of a power function:

$$251 \quad \frac{\partial a}{\partial D} = N \frac{a}{D} \quad (18)$$

252 which when combined with (16) to evaluate (15) yields:

$$253 \quad \frac{d\bar{Q}}{dt} \cong \frac{\phi}{\tau} (1 + N) \frac{d\bar{\eta}}{dt} \quad (19)$$

254 where  $\partial\bar{Q}/\partial t = 0$  for clarity. In this case, (19) can be rearranged and linearized around a  
255 reference  $\tau$  to express  $d\bar{\eta}/dt$  in terms of  $d\bar{Q}/dt$ :

$$256 \quad \frac{d\bar{\eta}}{dt} = \frac{\tau_r}{\phi} \left( \frac{1}{N + 1} \right) \frac{d\bar{Q}}{dt} \quad (20)$$

257 where  $\tau_r$  is a reference  $\tau$  taken at a reference time, or as an average value over a reference  
258 period, and  $\lambda = \tau_r/\phi[1/(N + 1)]$  is a (linearized) sensitivity coefficient.

259 As an alternative to (15), the long-term change in active layer thickness can be expressed  
260 in terms of the direct dependence between  $a$  and  $D$ :

$$261 \quad \frac{da}{dt} = \frac{da}{dD} \frac{dD}{dt}. \quad (21)$$

262 Rearranging in terms of  $D$  and substituting (18) yields, upon linearization:

$$263 \quad \frac{d\bar{\eta}}{dt} = \frac{\eta_r}{a_r} \left( \frac{1}{N} \right) \frac{da}{dt} \quad (22)$$

264 where  $\eta_r$  and  $a_r$  are reference values as previously described.

265 Noting that  $N = 3 - 2b$  for all but two sloped-aquifer solutions (Rupp & Selker, 2006b),  
266 we can write particular forms of (20) and (22):

$$267 \quad \frac{d\bar{\eta}}{dt} = \frac{\tau}{\phi} \left( \frac{1}{4 - 2b} \right) \frac{d\bar{Q}}{dt} \quad (23)$$

268 and:

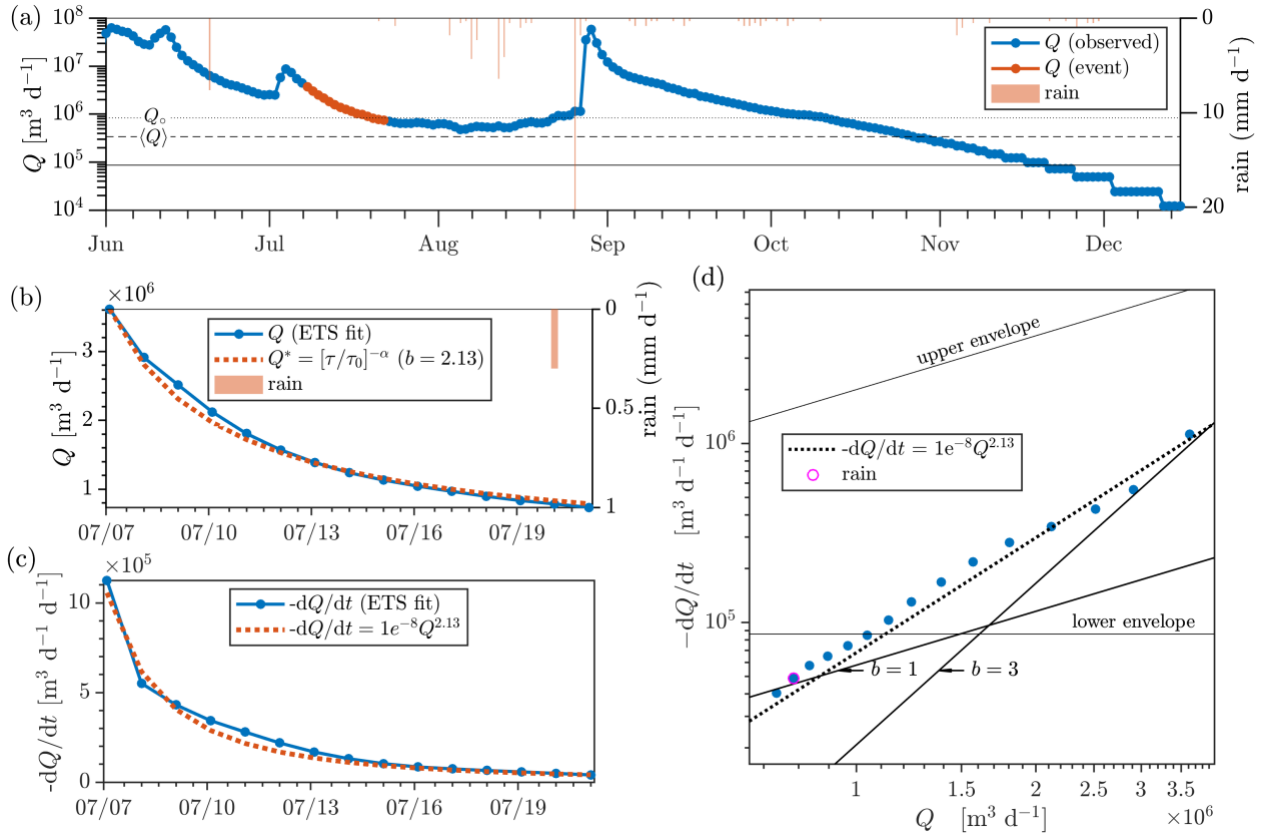
$$269 \quad \frac{d\bar{\eta}}{dt} = \frac{\eta}{a} \left( \frac{1}{3 - 2b} \right) \frac{da}{dt} \quad (24)$$

270 which recover Equation 10 and Equation 13 of Brutsaert and Hiyama (2012) for the linear case  
271  $b = 1$ .

272 In (24),  $\phi$  is contained within the definition of  $a$ , which is an advantage because  $\phi$  is  
273 highly uncertain (Lv et al., 2021). However, (24) requires a value for  $\eta_r$ , which may be  
274 unavailable (Brutsaert & Hiyama, 2012). In addition, (24) requires a reliable estimate of  $da/dt$ ,  
275 which can be difficult to obtain relative to  $d\bar{Q}/dt$ , because  $a$  is not observed.

#### 276 **4 Baseflow recession analysis**

277 Methods to estimate drainage timescale  $\tau$ , recession parameters  $a$  and  $b$ , and drainable  
278 porosity  $\phi$  are required before (20) can be applied to data. We designed a baseflow recession  
279 analysis algorithm for this purpose (Figure 3). The algorithm detects periods of declining flow  
280 (recession events) on quality-controlled streamflow timeseries, approximates  $dQ/dt$ , and fits (3)  
281 to estimate  $a$  and  $b$ . Event detection follows recommendations in Dralle et al. (2017),  $dQ/dt$  is  
282 estimated with an exponential time step (Roques et al., 2017), and nonlinear least-squares  
283 minimization is used to fit (3). In addition to the recommendations in Dralle et al. (2017), we  
284 exclude recession flows on days with recorded rainfall if  $dQ/dt$  attains a local maximum within  
285 a six-day window centered on the date of rainfall, that is, if a rainfall response is detected (Figure  
286 3b). The event-based  $a$ ,  $b$ , and  $Q$  values are then used to compute  $\tau(Q)$  for each event from (9),  
287 yielding a sample  $\tau$  population of size equal to the sample size of  $Q$ . Methods to estimate  
288 expected values of  $\tau$ ,  $b$ , and  $\phi$  are described in the following two sections.



289

**Figure 3:** Example application of baseflow recession algorithm: (a) daily streamflow  $Q$  during 1992 and one highlighted recession event on a logarithmic scale against time (left axis), and rainfall (vertical bars) on a linear scale (right axis). Horizontal lines are  $Q_0$  (dotted),  $\langle Q \rangle$  (dashed), and minimum observable  $-dQ/dt$  (solid) dictated by the streamflow precision (Rupp & Selker, 2006a) (value shown is  $1 \text{ m}^3 \text{ s}^{-1} \text{ d}^{-1}$ ; actual precision varies). (b-c) Estimated  $Q$  and  $-dQ/dt$  computed with an exponential time step (ETS) (Roques et al., 2017) compared to predictions from Equation (10) and Equation (3) using best-fit parameters  $a$  and  $b$ . (d) Point-cloud diagram with non-linear least squares fit to Equation (3), rainfall (open circles), and four reference lines: the “upper-envelope” (line of slope  $b = 1$  and intercept  $a = 2$ ) represents the maximum  $-dQ/dt$  for given  $Q$  dictated by the daily timestep (Rupp & Selker, 2006a), “lower-envelope” (horizontal line) represents the minimum observable  $-dQ/dt$  ( $\sim 86400 \text{ m}^3 \text{ d}^{-1} \text{ d}^{-1}$ ), line of slope  $b = 1$  passing through the 5<sup>th</sup> percentile of  $-dQ/dt$  represents the theoretical late-time fit, and a line of slope  $b = 3$  passing through the 95<sup>th</sup> percentile of  $-dQ/dt$  represents the theoretical early-time fit. The permissive rainfall filter retains streamflow unless rainfall exceeds  $1 \text{ mm d}^{-1}$  and  $-dQ/dt$  attains a local maximum within a three-day window.

304

#### 4.1 Estimating drainage timescale $\tau$ and recession parameters $a$ and $b$

305

306

307

308

309

As described in Section 2.2, the probability density function  $p(\tau)$  follows a Pareto distribution, unlike  $p(Q)$  which can be shown to follow the  $q$ -exponential distribution of non-extensive statistical mechanics (Tsallis, 1988). Both distributions are associated with power law scaling. An advantage of the Pareto transformation over the  $q$ -exponential is that widely-used and thoroughly vetted algorithms are available to fit the distribution, including the

310 lower-bound  $\tau_0$  (Clauset et al., 2009; Hanel et al., 2017). In particular, an expression for the  
 311 maximum likelihood estimate of  $\hat{a}$  exists in closed form. This means  $\hat{\tau}_0$  can be found by a global  
 312 search over all  $\tau_0 \in \tau$  for the value that minimizes a measure of distance between the data and  
 313 Pareto distribution fit to  $\tau \geq \tau_0$ . We applied a widely-used algorithm that minimizes the  
 314 Kolmogorov-Smirnoff distance to estimate  $\hat{\tau}_0$  (Clauset et al., 2009).

315 The Pareto distribution fit to  $p(\tau)$  also provides an unbiased estimate of  $\hat{b}$  via the  
 316 relationship:

$$317 \quad b = 1 + 1/\alpha, \quad (25)$$

318 see (10)–(13). Equation 25 provides a method to estimate  $b$  in lieu of ordinary least-squares  
 319 fitting to a bi-logarithmic plot of  $Q$  versus  $-dQ/dt$  (i.e., the “point cloud”). In contrast, the  
 320 parameter  $a$  is not provided by this procedure. Although we only require  $a$  at the scale of  
 321 individual recession events to estimate  $\tau(Q)$ , it is useful to have a global estimate, call it  $\hat{a}$ , to  
 322 maintain analytical consistency with  $\hat{b}$  and  $\hat{\tau}_0$  when estimating quantities such as  $\phi$  (Section  
 323 4.2). We estimated  $\hat{a}$  by constraining a line of slope  $\hat{b}$  to pass through the centroid of the  $\tau \geq \hat{\tau}_0$   
 324 point cloud. This procedure is illustrated graphically in Section 5, where analogous procedures  
 325 are used to estimate  $\hat{Q}_0$  and  $\langle Q \rangle$ , but can be defined mathematically as:  $\hat{a} = \overline{\log[-dQ/dt]} -$   
 326  $\hat{b} \overline{\log[Q]}$ , where overbars indicate geometric averages of the respective quantities within the  
 327 sample space  $\tau \geq \hat{\tau}_0$ .

328 In practice, once  $\hat{\tau}_0$  was determined, the Pareto fit was repeated 1000 times by bootstrap  
 329 resampling with replacement from the underlying  $\tau \geq \hat{\tau}_0$  sample. Reported parameters are  
 330 averages of the bootstrapped parameter ensemble. Uncertainties are presented as 95% confidence  
 331 intervals (~two standard deviations).

## 332 **4.2 Estimating drainable porosity $\phi$**

333 Estimates of  $\phi$  were obtained from a method proposed by Brutsaert and Nieber (1977). In  
 334 this approach, an early-time expression for  $a$  is substituted into a late-time solution and common  
 335 terms are eliminated, leaving  $\phi$  as the sole unknown. Taking the early-time solution ( $b = 3$ )  
 336 from Polubarinova-Kochina (1962) and the linearized late-time solution ( $b = 1$ ) from  
 337 Boussinesq (1903), we find:

338 
$$\phi = \frac{1}{DA} \left( \frac{c_1}{a_1} \right)^{1/2} \left( \frac{c_2}{a_2} \right)^{1/2}, \quad (26)$$

339 where  $DA$  is an effective aquifer volume,  $a_1$  and  $a_2$  are the respective early- and late-time  
 340 estimates of  $a$ ,  $c_1 = 1.133$ , and  $c_2 = \pi^2 p$ , where  $0 < p \leq 1$  linearizes the water table variation  
 341 during aquifer drawdown and in the context of (26) is assigned a value  $p = 1/3$  (Brutsaert &  
 342 Nieber, 1977). Using the nonlinear late-time solution ( $b = 3/2$ ) from Boussinesq (1904), we  
 343 find:

344 
$$\phi = \frac{1}{DA} \left( \frac{c_1}{a_1} \right)^{1/3} \left( \frac{c_2}{a_2} \right)^{2/3}, \quad (27)$$

345 where again  $c_1 = 1.133$  and  $c_2 = 4.804$ . The same approach with the nonlinear early- and  
 346 late-time solutions for a power-function  $k(z)$  profile (Rupp & Selker, 2005) (hereafter RS05)  
 347 yields:

348 
$$\phi = \frac{1}{DA} \left( \frac{c_1}{a_1} \right)^{\frac{1}{n+3}} \left( \frac{c_2}{a_2} \right)^{\frac{1}{n+3}}, \quad (28)$$

349 where:

350 
$$c_1 = f_{R1}, \quad c_2 = \frac{(f_{R2})^{n+2}}{2^n(n+1)}, \quad -1 < n \quad (29)$$

351 and  $f_{R1}$  and  $f_{R2}$  are parameters related to the Beta function evaluated at  $n + 2$  and 2, and  $(n +$   
 352  $2)/(n + 3)$  and  $1/2$ , as defined by Equation 26 and Equation 49 of RS05, respectively.

353 Although the late-time RS05 solution for a power-function  $k(z)$  profile was derived  
 354 under the assumption  $0 \leq n$ , the solution appears valid on  $-1 < n$ , where  $b$  ranges from 1 to 2  
 355 as  $n$  varies from  $-1$  to  $+\infty$  (and  $a \rightarrow +\infty$  at  $n = -1$ ). However, values of  $-1 < n < 0$  predict  
 356 an inverted  $k(z)$  profile given (5). One benefit of (28), therefore, is its compatibility with any  
 357 late-time value  $3/2 \leq b < 2$ , or with  $1 < b < 2$  if an inverted  $k(z)$  profile is acceptable,  
 358 whereas (26) and (27) assume late-time  $b = 1$  and  $b = 3/2$ , respectively.

359 We tested two methods to estimate  $a_1$  and  $a_2$  for application of (26)–(28). In the first  
 360 method, a line of slope  $b = 3$  was fit through the 95th percentile of the  $Q$  point-cloud to  
 361 approximate early-time  $a_1$ , and lines of slope  $b = 1$ ,  $b = 3/2$ , and  $\hat{b}$  were fit through the  $\tau \geq \hat{\tau}_0$

362 point cloud to approximate late-time  $a_2$ . For the latter estimate,  $a_2 = \hat{a}$  as described in Section  
 363 4.1. The second method was similar to the first, except that  $a_1$  and  $a_2$  were fit to each individual  
 364 event rather than the point cloud. This resulted in a sample of  $\phi$  values to which we fit a Beta  
 365 distribution, which is appropriate for random variables defined on  $(0,1)$ . Reference values for  
 366 catchment area  $A = 8400 \text{ km}^2$ , drainage network length  $L = 320 \text{ km}$ , active layer thickness  $D =$   
 367  $0.5 \text{ m}$ , and slope  $\theta = 1.15^\circ$  were used in each case, where  $\theta$  was chosen to be consistent with  
 368 the mean catchment elevation ( $\sim 265 \text{ m}$ ) and a characteristic hillslope breadth  $B = 13 \text{ km}$  using  
 369 the relationship  $B = A/(2L)$ .

### 370 4.3 Statistical uncertainty

371 Unless stated otherwise, all statistical uncertainties reported in this paper correspond to  
 372 95% confidence intervals around the mean. In addition, we include second-order interaction  
 373 terms because  $\tau$ ,  $\phi$ , and  $b$  are not independent. As described later, the error distributions on  $\tau$ ,  $\phi$ ,  
 374 and  $b$  satisfy the normality assumption required by the following error propagation method  
 375 (Taylor & Kuyatt, 1994).

376 The primary quantitative prediction made in this paper is the average rate of change of  
 377 the active groundwater layer,  $d\bar{\eta}/dt$ , estimated via (23). To estimate the statistical uncertainty of  
 378  $d\bar{\eta}/dt$  we combined the individual uncertainty estimates of each term in (23):

$$379 \quad \hat{\varepsilon}_{d\bar{\eta}/dt} = d\bar{\eta}/dt \sqrt{\left(\frac{\hat{\varepsilon}_\lambda}{\lambda}\right)^2 + \left(\frac{\hat{\varepsilon}_{d\bar{Q}/dt}}{d\bar{Q}/dt}\right)^2}, \quad (30)$$

380 where:

$$381 \quad \hat{\varepsilon}_\lambda = \sqrt{\mathbf{J} \mathbf{V} \mathbf{J}^T} \quad (31)$$

382 is the uncertainty of the sensitivity coefficient  $\lambda = \tau/\phi[1/(N + 1)]$ ,  $\mathbf{J}$  is the Jacobian of  $\lambda$ ,  $\mathbf{V}$  is  
 383 the covariance matrix of the sample populations  $\{\tau, \phi, N\}$ , and  $\hat{\varepsilon}_{d\bar{Q}/dt}$  is the uncertainty of the  
 384 trend slope  $d\bar{Q}/dt$  estimated via ordinary least-squares linear regression. Recall  $N \sim 1/(2b)$  in  
 385 (23) therefore  $\hat{\varepsilon}_N = 2\hat{\varepsilon}_b$ .

## 386 **5 Application of theory to Kuparuk River Basin streamflow and active layer thickness data**

### 387 **5.1 Surface-based observational data**

388 In this section, the theory proposed in Section 3 and Section 4 is applied to 38 years of  
389 daily streamflow data for the Kuparuk River on the North Slope of Arctic Alaska (70°16'54"N,  
390 148°57'35"W) (Figure 2). The Kuparuk River drains an ~8400 km<sup>2</sup> catchment area that extends  
391 from the foothills of the Brooks Range northward to the Arctic Ocean along the Central Beaufort  
392 Coastal Plain. Catchment topography is characterized by low relief with mean elevation ~265 m  
393 a.s.l. and elevation range 10–1500 m a.s.l.. Catchment soils are comprised of alluvial marine and  
394 floodplain deposits and aeolian sand and loess, underlain by continuous permafrost >250 m  
395 thick. The Kuparuk basin-mean active layer thickness is thought to be less than one meter on  
396 average (McNamara et al., 1998; O'Connor et al., 2019).

397 Water levels were recorded at United States Geological Survey (USGS) gage 15896000  
398 and converted to discharge by USGS personnel following USGS protocols (Rantz, 1982). Daily  
399 flows are reported to nominal 1 ft<sup>3</sup> s<sup>-1</sup> precision. Stage and discharge accuracy are affected by  
400 fluvial incision and landscape degradation, by river ice and aufeis during winter (Huryn et al.,  
401 2021), and by ice jams and flooding during ice breakup. Annual USGS water-year summaries  
402 indicate automated ratings are replaced by estimated values due to aforementioned factors, and  
403 the actual precision of reported discharge varies from ~0.1 ft<sup>3</sup> s<sup>-1</sup> for automated ratings to ~1000  
404 ft<sup>3</sup> s<sup>-1</sup> for estimated values.

405 Stage and discharge precision together define a minimum observable  $-dQ/dt$  which may  
406 impart bias on estimated recession parameters (Rupp & Selker, 2006a). The effect of  
407 measurement precision for Kuparuk River flows is evident in estimated flow values below ~100  
408 ft<sup>3</sup> s<sup>-1</sup> (~2.5e<sup>5</sup> m<sup>3</sup> d<sup>-1</sup>), which typically occur during Oct–Nov prior to flow cessation from ~Dec–  
409 May (Figure 3a). The rapid flow increase following river ice breakup in late Spring partially  
410 masks the discretization of low-precision estimated values. As mentioned in Section 4.2,  
411 measurement discretization was remediated by use of an exponential time step to compute  
412  $dQ/dt$  (Roques et al., 2017). Note all flow data is converted to m<sup>3</sup> d<sup>-1</sup> prior to fitting (3).

413 Active layer thickness is measured at nine locations within the Kuparuk River basin  
414 (Figure 2) (Nyland et al., 2021). The measurements used here were made by inserting  
415 small-diameter metal probes to point of refusal at regular intervals along grids or transects of

416 side-length ~100–1000 m. Mechanical probing is supplemented by thermistors measuring soil  
417 temperature at four sites. Data are reported as end-of-season averages believed to represent the  
418 annual maximum thaw depth (i.e., *ALT*). A continuous annual record from 1990–2020 is  
419 available for the Toolik Long Term Ecological Reserve site, from 1992–2020 for the Innvait  
420 Creek site, and from 1995–2020 for other sites; all site data were averaged to create one  
421 continuous record for the Kuparuk River basin. The CALM program and the International  
422 Permafrost Association implemented standardized measurement protocols around 1995.

423         Precipitation is measured at a network of meteorological stations within and proximate to  
424 the catchment (Kane et al., 2021). Although gauge undercatch affects Arctic precipitation  
425 measurements, our goal is to determine if rainfall occurred rather than how much occurred, and  
426 undercatch is small (~10%) during the late summer recession period when wind speeds are lower  
427 (Yang et al., 2005). Daily precipitation measurements from 1983–2020 used in this study were  
428 measured at the National Oceanic and Atmospheric Administration Cooperative Observer  
429 Program station 505136 (Kuparuk station).

## 430         **5.2 Topographic data**

431         Catchment topography was provided by USGS digital terrain models for the state of  
432 Alaska derived from interferometric synthetic aperture radar (IFSAR) (Earth Resources  
433 Observation And Science (EROS) Center, 2018). These data were provided as tiles with  
434 elevations posted at 5 m horizontal resolution and clipped to the catchment outline using the  
435 Geospatial Data Abstraction software Library (Figure 2) (GDAL/OGR contributors, 2022).

## 436         **5.3 Climate reanalysis and satellite observations**

437         Climate reanalysis and satellite gravimetry data were used to close the annual water  
438 balance, which provides a method to infer permafrost thaw rate (Brutsaert & Hiyama, 2012).  
439 Climate reanalysis was provided by Modern-Era Retrospective Analysis for Research and  
440 Applications, version 2 (MERRA2) (Gelaro et al., 2017). Monthly terrestrial water storage  
441 anomalies were provided by University of Texas at Austin Center for Space Research CSR RL06  
442 Gravity Recovery and Climate Experiment (GRACE) and GRACE Follow-On (GRACE-FO)  
443 mascon solutions (<http://www2.csr.utexas.edu/grace>) (Save et al., 2016). GRACE data is  
444 available on a monthly timestep for the period 2002–2020. Twenty-two missing values in the

445 GRACE timeseries and thirteen GRACE-FO values were gap-filled following Yi and Sneeuw,  
446 (2021).

447 The annual liquid water balance is defined as:

$$448 \quad \frac{dS_\ell}{dt} = P - E - R + T \quad (32)$$

449 where  $P$ ,  $E$ , and  $R$  ( $L/T$ ) are annual sums of precipitation, evaporation, and runoff fluxes, and  $T$   
450 ( $L/T$ ) is a source term representing the catchment-mean permafrost thaw rate:

$$451 \quad T = - \left( \frac{\rho_{\text{ice}}}{\rho_w} \right) \frac{d\theta_{\text{ice}}}{dt} \quad (33)$$

452 where  $\rho_{\text{ice}}$  [ $M/L^3$ ] is ice density,  $\rho_w$  [ $M/L^3$ ] is liquid water density, and  $\theta_{\text{ice}}$  [ $L^3/L^3$ ] is volumetric  
453 soil ice content (the ratio of ice by volume to soil by volume).

454 GRACE water storage anomalies do not measure  $dS_\ell/dt$  (32) but rather  $(P - E - R)$   
455 (and any other gain or loss of above- or below-ground mass). In contrast,  $\phi d\bar{\eta}/dt$  as predicted  
456 via (20) is, in principle, comparable to (32), which shows that  $d\bar{\eta}/dt$  is only attributable to  $T$  if  
457  $(P - E - R) = 0$ . Therefore, we can attempt to detect  $T$  by rearranging (32):

$$458 \quad T = \frac{dS_B}{dt} - (P - E - R) \quad (34)$$

459 where  $S_B = S - S_{\text{ref}}$  is storage anomaly at time  $t$  detected with baseflow recession analysis as in  
460 (6). Alternatively:

$$461 \quad T = \frac{dS_B}{dt} - \frac{dS_G}{dt} \quad (35)$$

462 where  $S_G$  is GRACE terrestrial water storage anomaly at time  $t$ .

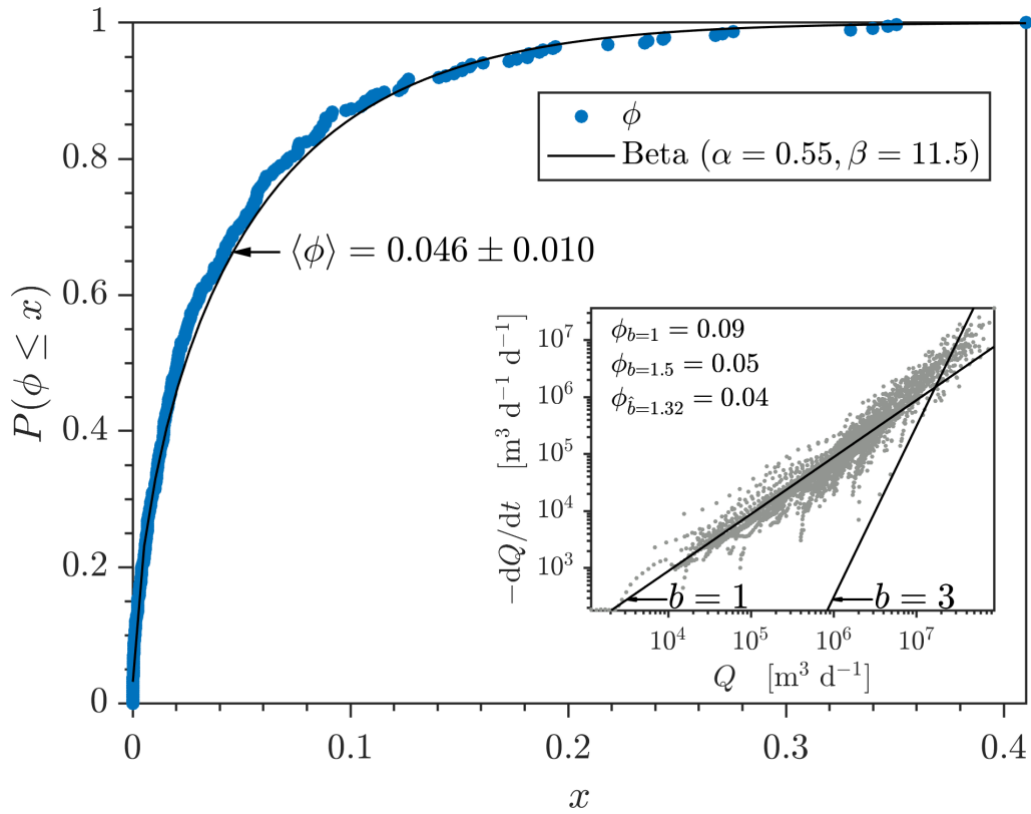
463 In practice,  $dS_B/dt$  was estimated by bringing  $\phi$  to the left-hand side of (20) and  
464 regressing the right-hand side  $\tau_r/(N + 1)\bar{Q}$  against time in years. Similarly,  $dS_G/dt$  was  
465 estimated via regression of annual August–October minimum  $S_G$  anomalies (which is used as a  
466 proxy for catchment storage during the streamflow recession period) against time in years. In this  
467 way, both (34) and (35) yield estimates of the average thaw rate  $T$  over the time interval  
468 represented by  $dt$ , which ranges from 18–37 years for  $S_B$ , and 18 years for  $S_G$  (Section 5.4.3).  
469 For 16 out of 19 years, the annual minimum  $S_G$  occurred in August–October, which coincides

470 with the streamflow recession period. In 2018,  $S_G$  reached a minimum in January and then a  
 471 second local minimum in September. Similarly, in 2010 and 2019  $S_G$  reached local minima in  
 472 November and July, respectively, with magnitudes nearly identical to adjacent October and  
 473 August values. To obtain a comparable estimate of  $dS/dt$  from MERRA2 reanalysis, we  
 474 compute  $(P - E - R)$  on a water year basis such that  $(P - E - R)_i$  represents  $dS/dt$  over a  
 475 period from October 1 of year  $i - 1$  to September 30 of year  $i$ .

## 476 **5.4 Comparison of theory with data in the Kuparuk River basin**

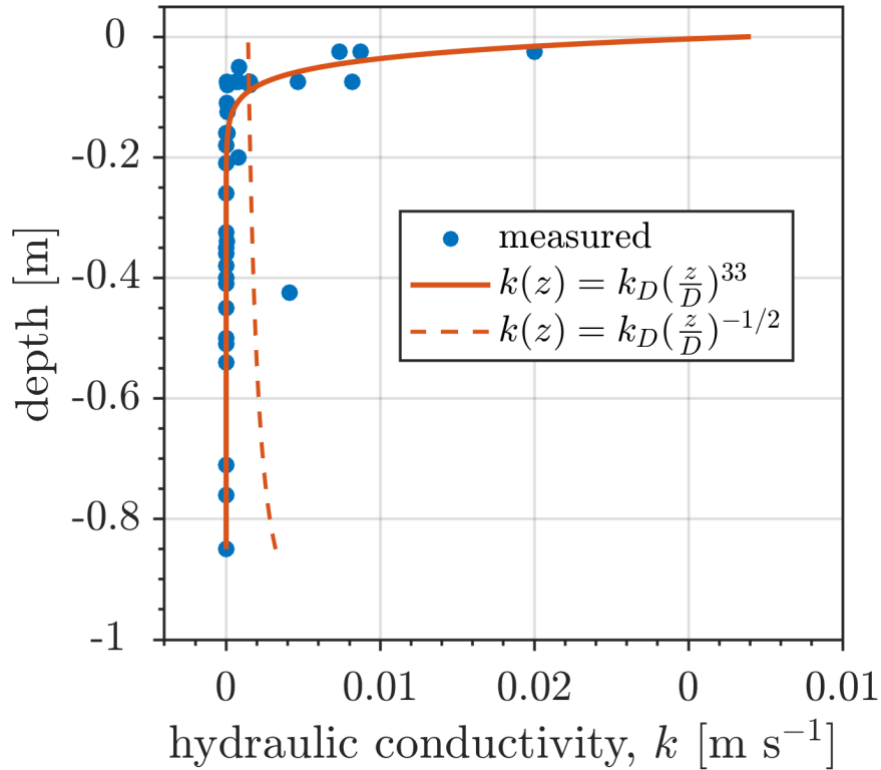
### 477 **5.4.1 Drainable porosity**

478 Estimates of  $\phi$  obtained from the point-cloud method and the event-based method  
 479 indicate a characteristic value of  $\langle\phi\rangle \cong 0.05$ , with moderate sensitivity to (26)–(28) (Figure 4).  
 480 Substitution of the respective point-cloud intercepts  $a_1$  and  $a_2$  into (26)–(28) yielded  $\phi =$   
 481  $0.04 - 0.09$ , depending on late-time  $b = 1$ ,  $b = 3/2$ , and  $\hat{b} = 1.32$  (Section 4.2). The  
 482 event-based method yielded a narrower range of values between 0.03–0.05 with relative  
 483 uncertainties of ~30–50% (Figure 4). Note that  $\hat{b} = 1.32$  implies an inverted  $k(z)$  profile in the  
 484 context of (5) with  $n \cong -1/2$ , which is inconsistent with field observations of  $k(z)$  in the upper  
 485 Kuparuk River basin (Figure 5) (O’Connor et al., 2019). Estimates based on (28) may therefore  
 486 be unreliable. To mitigate this, we construct an estimate based on (26) and (27). The justification  
 487 is that  $b = 1$  and  $b = 3/2$  bracket  $\hat{b} = 1.32$  without assuming an inverted  $k(z)$  profile.  
 488 Combining all event-based  $\phi$  values from (26) and (27) into one sample, we obtain a Beta  
 489 distribution fit  $\langle\phi\rangle \cong 0.046 \pm 0.009$  (Figure 4), which is used in all results hereafter.



490

491 **Figure 4:** (main panel) Cumulative probability distribution of drainable porosity  $\phi$  estimated from  
 492 individual recession events with Equation 26 and Equation 27 (blue circles) and the best-fit Beta  
 493 distribution (solid black line). The expected value of  $\phi$  is indicated by arrow. (inset) Example of the  
 494 point-cloud method to estimate  $\phi$  with Equations 26–28, using values of early-time intercept  $a_1$  for a line  
 495 of slope  $b = 3$ , and late-time intercept  $a_2$  for lines of slope  $b = 1$ ,  $b = 3/2$ , and  $\hat{b} = 1.32$  (inset shows  
 496  $b = 3$  and  $b = 1$  for demonstration;  $\phi$  estimated with each of Equations 26–28 are printed upper left).  
 497

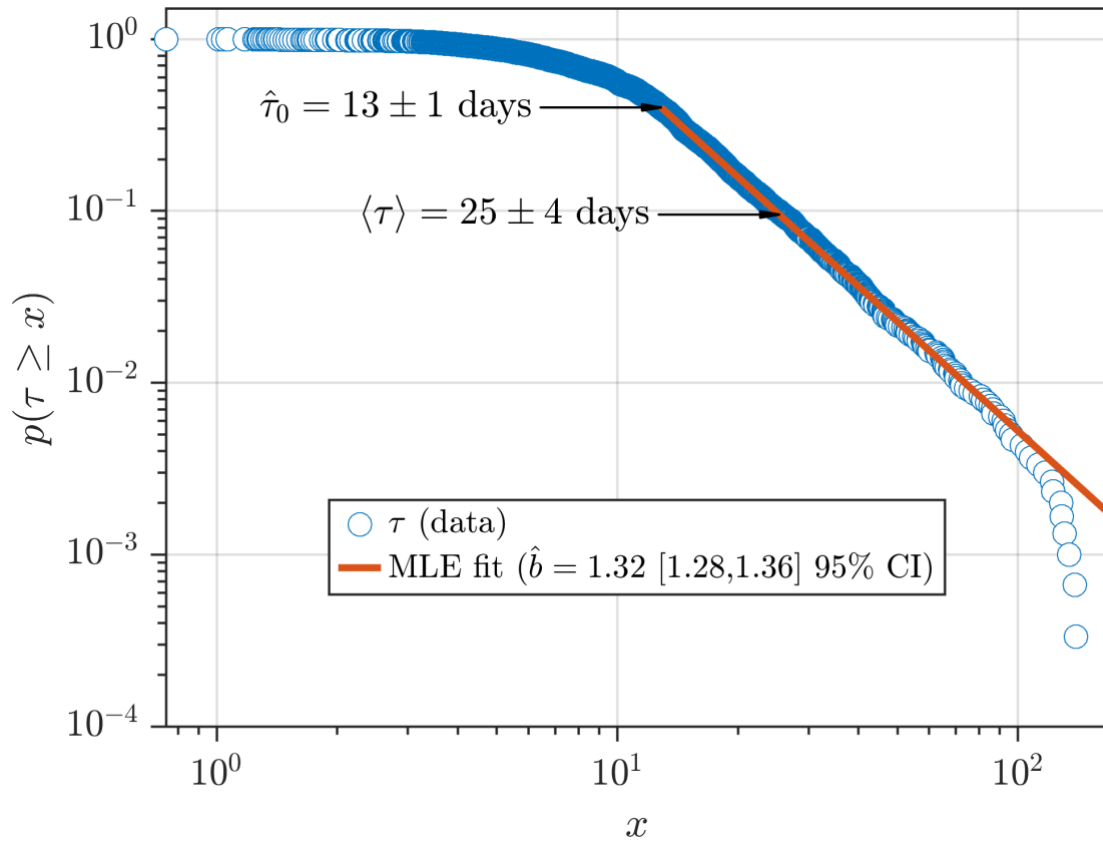


498

499 **Figure 5:** Saturated hydraulic conductivity (solid circles) measured at Imnavait Creek Research Station in  
 500 the Kuparuk River basin (O'Connor et al., 2019) and the best-fit nonlinear least-squares power-function  
 501 (solid line). The best-fit exponent  $n \cong 33$  corresponds to  $b = 1.97$  for both flat- and sloped-aquifer  
 502 solutions ( $b \rightarrow 2$  for  $n \gg 10$  for both solutions). The best-fit value obtained from recession analysis  $\hat{b} =$   
 503  $1.32$  ( $n \cong -1/2$ ) predicts an inverted saturated hydraulic conductivity profile (dashed line), which is  
 504 inconsistent with the measurements.

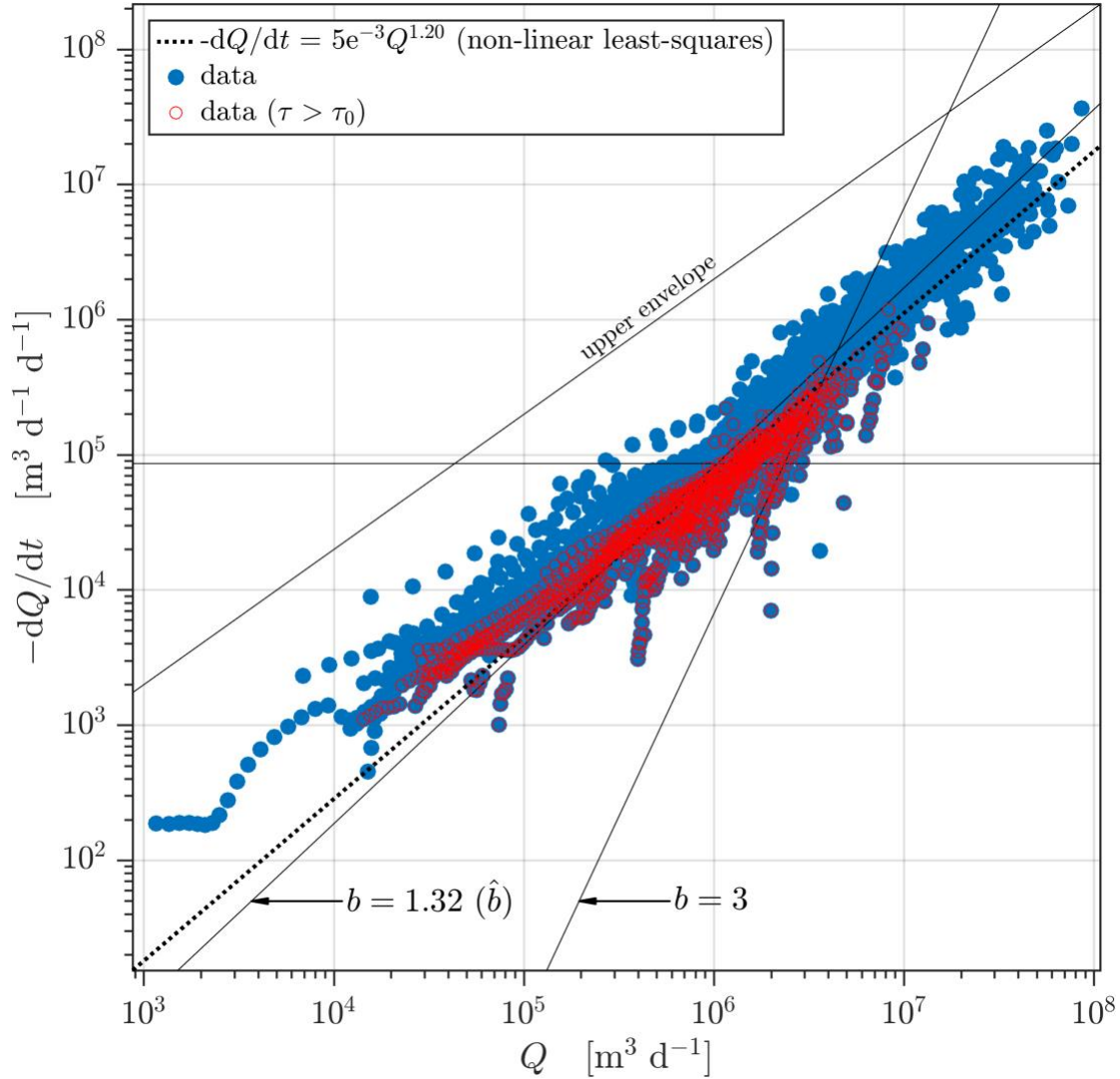
#### 505 5.4.2 Drainage timescale and expected value of baseflow

506 The Pareto distribution fit to  $\tau$  yielded an estimate of  $\hat{\tau}_0 = 13 \pm 1$  days and  $\langle \tau \rangle = 25 \pm 4$   
 507 days (Figure 6). The estimated exponent  $\hat{\alpha} = 3.11 \pm 0.44$  corresponds to  $\hat{b} = 1.32 \pm 0.04$ . A  
 508 total of 3,010  $\tau$  values were obtained from 186 recession events, of which 1,203 values exceeded  
 509  $\tau_0$  (Figure 7, red circles). Note that an individual  $\tau$  value may exceed  $\tau_0$  but occur within an  
 510 event of duration  $t < \tau_0$  (96 events exceeded  $\hat{\tau}_0$  in duration). The  $\hat{\alpha}$ ,  $\hat{\tau}_0$  and  $\langle \tau \rangle$  parameter  
 511 ensembles constructed by bootstrap resampling (Section 4.1) from the 1,203  $\tau \geq \hat{\tau}_0$  values were  
 512 symmetric about the mean to within the  $\sim$ one-day and  $\sim$ four-day precision.



513

514 **Figure 6:** Complementary cumulative (exceedance) probability for drainage timescale  $\tau$  (blue circles) and  
 515 the maximum likelihood estimate (MLE) best-fit Pareto distribution (solid red line). The theoretical  
 516 distribution (Equation 12) is fit to  $\tau > \tau_0$ , where  $\tau_0 = 13$  days is the threshold timescale beyond which  
 517 baseflow scales as a power-law. The expected value  $\langle \tau \rangle = 25$  days is the average drainage timescale  
 518 given the best-fit parameter  $\hat{b} = 1.32$ . Confidence intervals are two standard deviations of a bootstrapped  
 519 ensemble ( $N=1000$ ). The falloff at  $\tau > 100$  days is indicative of finite system size effects which occur  
 520 when the underlying population is under-sampled at extreme values but may also indicate a process  
 521 transition to linear scaling as  $Q \rightarrow 0$ .  
 522



523

524 **Figure 7:** Point-cloud diagram showing 3,010 values of  $Q$  and  $-dQ/dt$  from 186 detected recession  
 525 events and a line of slope  $\hat{b} = 1.32$  obtained from  $b = 1 + 1/\alpha$  (Equation 25) compared with a line of  
 526 slope  $b = 1.20$  (dotted) obtained from nonlinear least-squares fit to the point cloud. Values of  $Q \in (\tau >$   
 527  $\tau_0)$  are highlighted with red circles. Reference lines are described in Figure 3.

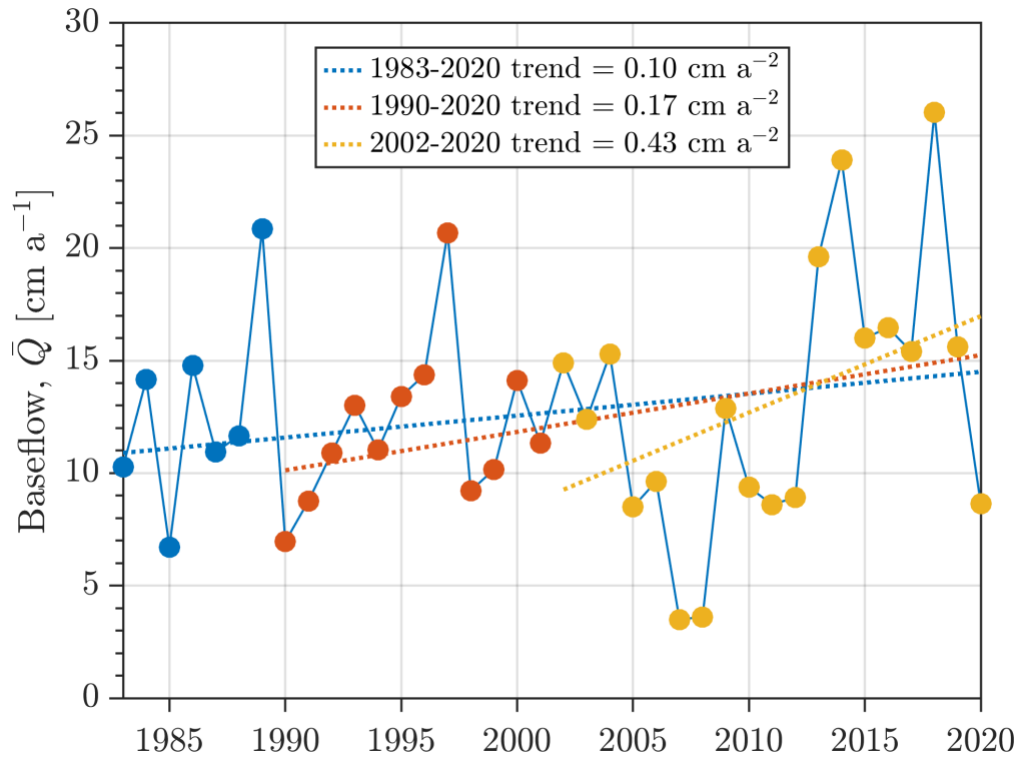
528

The Pareto fit to  $\tau$  does not provide  $\langle Q \rangle$  nor  $\hat{Q}_0$ , although they could be obtained from a  
 529 similar modeling procedure. Instead, a value of  $\hat{Q}_0 = 10 \text{ m}^3 \text{ s}^{-1}$  (Figure 3a, dotted line) consistent  
 530 with  $\hat{\tau}_0 = 13$  days and  $\hat{b} = 1.32$  was obtained from (9), similar to the method used to obtain  $\hat{a}$   
 531 (Section 4.1). In this context,  $\hat{Q}_0$  is an estimate of the threshold value of  $Q$  below which baseflow  
 532 scales as a power-law, and the theory outlined herein can be expected to make reasonable  
 533 predictions. The value  $10 \text{ m}^3 \text{ s}^{-1}$  maps to the 36<sup>th</sup> percentile of the daily flow and is similar to the  
 534 mean October flow  $\sim 13 \text{ m}^3 \text{ s}^{-1}$ . From (13), it predicts a value for expected baseflow  $\langle Q \rangle = 3.6 \text{ m}^3$

535  $s^{-1}$ , which maps to the 26<sup>th</sup> percentile of daily flow (Figure 3a, dashed line). The mean daily flow  
536 is  $\sim 80 \text{ m}^3 \text{ s}^{-1}$ .

537 On this basis, the long-term baseflow trend  $d\bar{Q}/dt$  was estimated by quantile regression  
538 on the 26<sup>th</sup> percentile of the annual timeseries of mean daily flow (Figure 8). That is,  $d\bar{Q}/dt$  is  
539 the trend in the flow percentile nearest  $\langle Q \rangle$ , the expected value of baseflow. Although we would  
540 prefer to estimate  $d\bar{Q}/dt$  from an annual timeseries of  $\langle Q \rangle$ , there is insufficient data to fit (12) on  
541 an annual basis. The baseflow timeseries is hereafter  $\bar{Q}$ , but it should be recognized that  $\bar{Q}$  is the  
542 26<sup>th</sup> percentile of the annual timeseries of mean daily flow.

543



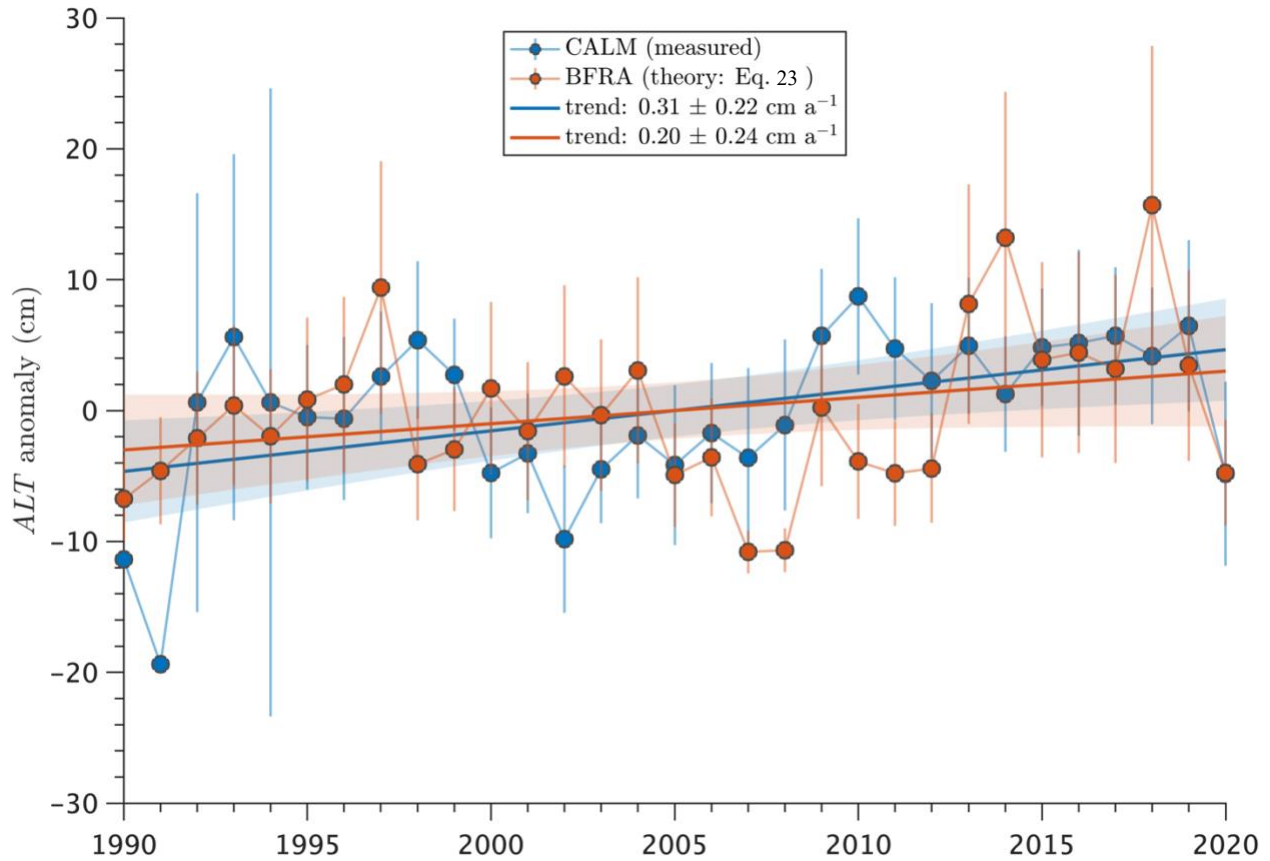
544  
545

546 **Figure 8:** Linear trend in the 26<sup>th</sup> percentile of daily flow on an annual basis for three periods examined in  
 547 this study. The expected value of baseflow  $\langle Q \rangle = 3.6 \text{ m}^3 \text{ s}^{-1}$  ( $13 \text{ cm a}^{-1}$ ) corresponds to the 26<sup>th</sup> percentile  
 548 of daily flow and is used in this study as a proxy for annual average baseflow  $\bar{Q}$ . The 26<sup>th</sup> percentile of  
 549 daily flow is the value of the flow duration curve having an exceedance probability of  $1 - 0.26 = 0.74$ .

### 550 5.4.3 Active groundwater layer thickness from recession analysis and observations

551 Three periods are examined, as dictated by data availability: 1983–2020 covers the period  
 552 of overlapping precipitation and discharge measurements; 1990–2020 adds *ALT* measurements;  
 553 2002–2020 adds GRACE data. From 1983–2020, observed mean annual flow increased  $0.24 \pm$   
 554  $0.15 \text{ cm a}^{-2}$  and  $\bar{Q}$  increased  $0.10 \pm 0.10 \text{ cm a}^{-2}$  (Figure 8). From 1990–2020, these rates  
 555 increased to  $0.31 \pm 0.21 \text{ cm a}^{-2}$  and  $0.17 \pm 0.21 \text{ cm a}^{-2}$ , respectively. During this period,  
 556 measured *ALT* increased  $0.31 \pm 0.22 \text{ cm a}^{-1}$ , and  $\bar{\eta}$  estimated with (23) increased  $0.20 \pm 0.24$   
 557  $\text{cm a}^{-1}$  (Figure 9). Converted to liquid water thickness using  $\langle \phi \rangle$ , the trend in measured *ALT*  
 558 converts to an active layer infilling rate of  $0.014 \pm 0.010 \text{ cm a}^{-1}$ , ~55% larger than  $dS_B/dt =$   
 559  $0.009 \pm 0.011 \text{ cm a}^{-1}$  estimated with (23). This suggests the saturated groundwater layer  
 560 increased at a slower rate than the actual active layer, and a surplus of thaw water in excess of  
 561  $d\bar{\eta}/dt$  contributed to the observed increase in  $\bar{Q}$  during this period. Water balance trends are  
 562 reported in Section 5.4.4.

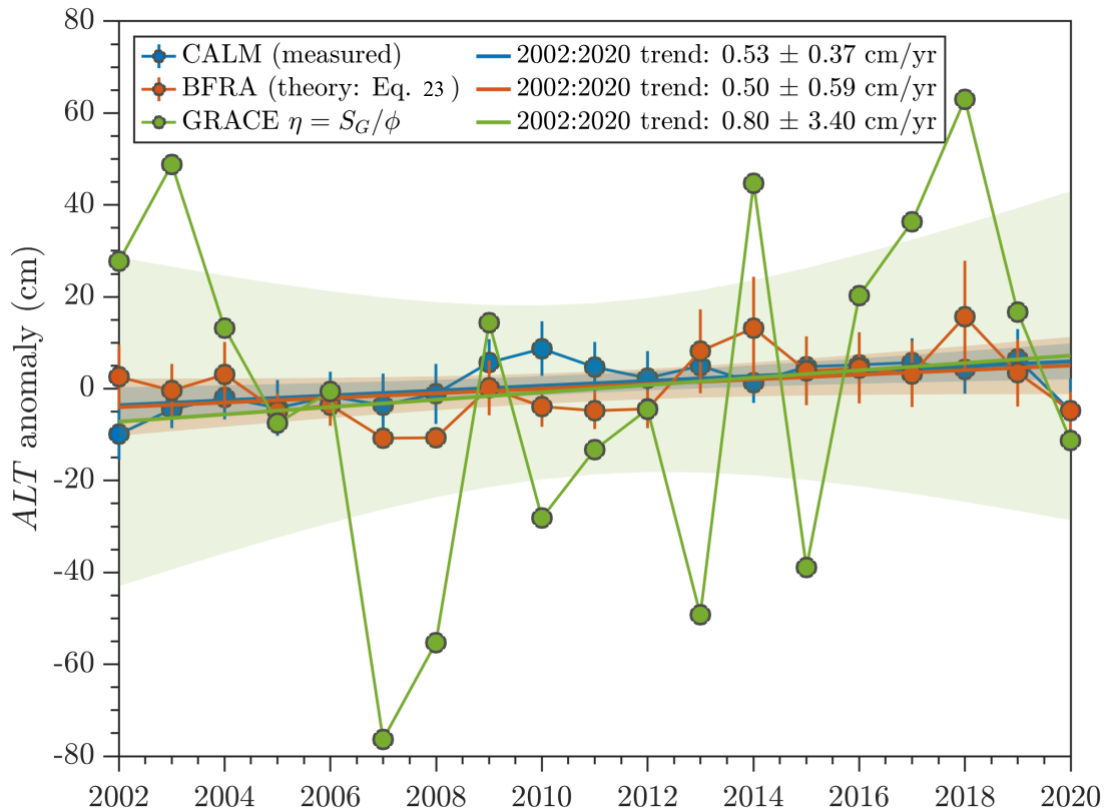
563

564  
565

566 **Figure 9:** Linear trend in active layer thickness from field measurements in the Kuparuk River basin  
 567 provided by the Circumpolar Active Layer Monitoring (CALM) program (Nyland et al., 2021) (blue error  
 568 bars and blue trend lines) compared with linear trend in active groundwater layer thickness predicted with  
 569 baseflow recession analysis (BFRA) (Equation 23) (red error bars and red trend lines). Error bars for  
 570 CALM data are two standard errors scaled by a critical t-value (95% confidence intervals); sample size  
 571 varies from one site (Toolik LTER) (1990 and 1991) to nine (1995–2020) as additional monitoring sites  
 572 were established. Error bars for BFRA predictions are 95% confidence intervals computed with Equation  
 573 (31) (Section 4.3). Shaded error bounds are 95% confidence intervals for the linear trend lines. Error  
 574 margins printed in the legend are 95% confidence intervals for the regression slope coefficients.

575 During 2002–2020, these trends approximately doubled (Figure 10). Measured *ALT*  
 576 increased  $0.53 \pm 0.37 \text{ cm a}^{-1}$ ,  $\bar{\eta}$  estimated with (23) increased  $0.50 \pm 0.59 \text{ cm a}^{-1}$ , and GRACE  
 577 terrestrial water storage converted to soil layer thickness via  $\eta_G = S_G/\phi$  increased  $0.80 \pm 3.4 \text{ cm}$   
 578  $\text{a}^{-1}$ . In terms of liquid water thickness, the observed *ALT* trend converts to an infilling rate  
 579  $0.024 \pm 0.017 \text{ cm a}^{-1}$ , ~5% higher than  $dS_B/dt = 0.023 \pm 0.027 \text{ cm a}^{-1}$  estimated with (23) and  
 580 ~34% lower than  $dS_G/dt = 0.036 \pm 0.15 \text{ cm a}^{-1}$ . The observed mean annual flow increased  
 581  $0.57 \pm 0.50 \text{ cm a}^{-2}$  and  $\bar{Q}$  increased  $0.43 \pm 0.50 \text{ cm a}^{-2}$  (Figure 8).

582



583

584 **Figure 10:** Linear trend in GRACE terrestrial water storage anomalies (green circles and green trend line)  
 585 and (as in Figure 9) active layer thickness from field measurements (blue error bars and blue trend lines)  
 586 compared with baseflow recession analysis predictions (red error bars and red trend lines). GRACE  
 587 storage anomalies are converted to equivalent groundwater layer thickness using  $\phi = 0.05$  inferred from  
 588 baseflow recession. Error bars and error bounds are described in Figure 9.

589

#### 5.4.4 Interpreting groundwater storage trends in terms of catchment water balance

590

591

592

593

594

595

596

597

598

As mentioned in Section 5.3, the trend in  $\bar{\eta}$  can only be attributed to permafrost thaw if  
 $P - E - R = 0$ . During 1990–2020, MERRA2 reanalysis indicates catchment-mean  $P$  increased  
 $0.22 \pm 0.29 \text{ cm a}^{-2}$ , balanced by an increase in  $E$  and  $R$  of  $0.01 \pm 0.07 \text{ cm a}^{-2}$  and  $0.21 \pm 0.23$   
 $\text{cm a}^{-2}$ , respectively, leaving a negligible residual trend in  $(P - E - R)$ . In this context, the  
 acceleration of  $P$  was balanced almost entirely by  $R$  and a small acceleration of  $E$ . However, the  
 annual average water-year  $(P - E - R)$  was  $\sim 1.04 \text{ cm a}^{-1}$ , well in excess of  $dS_B/dt$ . Strictly  
 speaking, this suggests  $dS_B/dt$  and  $d\bar{Q}/dt$  cannot be attributed to permafrost thaw during this  
 period, because the excess  $(P - E - R)$  is sufficient to explain all of the increase in  $S_B$  and  $\bar{Q}$ ,  
 and then some. This is discussed further in Section 6.

599

600

Turning to the GRACE period (2002–2020), MERRA2 reanalysis indicates  
 catchment-mean  $P$  increased  $0.59 \pm 0.68 \text{ cm a}^{-2}$ , balanced by an increase in  $E$  and  $R$  of  $0.05 \pm$

601 0.15 cm a<sup>-2</sup> and  $0.52 \pm 0.52$  cm a<sup>-2</sup>, respectively, leaving a residual acceleration in  $(P - E - R)$   
 602 of  $0.03 \pm 0.47$  cm a<sup>-2</sup>. The annual average water-year  $(P - E - R)$  was  $\sim 0.98$  cm a<sup>-1</sup>, again, well  
 603 in excess of  $dS_B/dt$ . However, these values are also well in excess of  $dS_G/dt = 0.036$  cm a<sup>-1</sup>, as  
 604 reported in Section 5.4.3. This appears robust: if  $dS_G/dt$  is approximated by annual differences  
 605 of annual-average  $S_G$  on a water-year basis (rather than linear regression),  $dS_G/dt = 0.06$  cm a<sup>-1</sup>.

606 We tested various alternative definitions of  $dS_G/dt$  including annual calendar-year  
 607 differences ( $dS_G/dt = 0.024$  cm a<sup>-1</sup>), annual differences of the annual maximum  $S_G$  ( $dS_G/dt =$   
 608  $0.25$  cm a<sup>-1</sup>), and annual differences of the average August–October  $S_G$  ( $dS_G/dt = -0.08$  cm  
 609 a<sup>-1</sup>). The largest values of  $dS_G/dt$  obtained were for Northern Hemisphere winter months, but  
 610 none approached the magnitude of MERRA2 water-year  $(P - E - R)$ . Subtraction of MERRA2  
 611 snow mass anomalies from  $S_G$  yielded different estimates of  $dS_G/dt$  but did not change the  
 612 conclusion that MERRA2  $(P - E - R)$  substantially exceeded both  $dS_G/dt$  and  $dS_B/dt$ .  
 613 Consequently, (34) is unlikely to provide meaningful estimates of  $T$ .

## 614 **6 Discussion**

### 615 **6.1 Active layer thickness and saturated soil layer thickness change**

616 We find that the saturated soil layer thickened between 1983–2020 in the Kuparuk River  
 617 basin, in agreement with field measurements of  $ALT$  in the region (Nyland et al., 2021). This  
 618 finding was enabled by new theoretical relationships between basin outflow during streamflow  
 619 recession and the rate of change of the active groundwater layer (Section 3), using the principles  
 620 of hydraulic groundwater theory (Brutsaert, 2005). Specifically, we extended an earlier linear  
 621 reservoir theory (Brutsaert & Hiyama, 2012) to the nonlinear case. This provides a physical  
 622 interpretation of the relationship between  $ALT$  trends and baseflow trends for river basins with  
 623 nonlinear empirical storage-discharge relationships. It is important to acknowledge that this  
 624 approach dramatically simplifies real-world permafrost hydrology, yet appears to provide  
 625 reasonable predictions for the studied area. Although a thorough comparison with more  
 626 observations is needed to build confidence, the framework developed here may open the door to  
 627 retrospective estimation of  $ALT$  trends in data sparse Arctic catchments with short, sporadic, or  
 628 even nonexistent ground-based active layer measurements.

629 A first application of the theory to 38 years of Kuparuk River streamflow indicates the  
630 active groundwater layer thickened ~4.4 cm during this time. The rate of increase nearly doubled  
631 between 1990–2020 for a total increase of ~6.2 cm. Direct measurements of the actual active  
632 layer thickness made during this period indicate an increase of ~9.6 cm. Although the plot-scale,  
633 site-averaged observed rate of change is +55% higher than the basin-scale theoretical prediction,  
634 both are consistent with observations of thickening active layer and a growing importance of  
635 subsurface hydrologic processes in the region (Arp et al., 2020; Luo et al., 2016; Rawlins et al.,  
636 2019; Rowland et al., 2011).

637 A similar picture emerged for the period 2002–2020, during which time observations of  
638 terrestrial water storage (TWS) from the GRACE and GRACE-FO satellites are available to aid  
639 interpretation. First, relative to 1990–2020, the inferred rate of increase of the active groundwater  
640 layer more than doubled again, in close agreement (+5%) with direct field measurements of the  
641 actual active layer thickness. In terms of liquid-water-equivalent storage, TWS anomalies  
642 increased ~50% more each year on average than predicted increases in active groundwater layer  
643 storage, albeit with uncertainties that exceed all reported trends. Under an idealized assumption  
644 that melted ice remains stored as liquid water (or is discharged and later replaced by  
645 precipitation) GRACE would detect no mass change. TWS trends are therefore not directly  
646 comparable to active groundwater layer storage trends predicted from baseflow recession, but  
647 rather indicate whether a surplus or deficit of water was available each year to support filling or  
648 draining of active layer.

649 Climate reanalysis and streamflow observations indicate that both precipitation and  
650 runoff are increasing in the Kuparuk River basin, at rates far exceeding inferred increases in  
651 water storage in thicker active layer over all periods examined. Focusing on 2002–2020,  
652 MERRA2 climate reanalysis indicates the annual average ( $P - E - R$ ) was positive ( $\sim 1 \text{ cm a}^{-1}$ ),  
653 and about twice as large when computed using observed discharge  $Q$  rather than climate  
654 reanalysis  $R$  (this holds over all periods examined). Moreover, the trend in MERRA2  $P$  outpaced  
655 the trend in  $E + R$  leaving a residual acceleration in ( $P - E - R$ ). The acceleration suggests a  
656 smaller ( $\sim 0.5 \text{ cm a}^{-1}$ ) average annual increase but remains an order of magnitude larger than  
657 predicted increases in active layer storage and TWS anomalies. Taken together, this suggests a  
658 surplus of precipitation was available to drive observed increases in discharge and storage in

659 thicker active layer, which precludes attribution of either discharge or *ALT* trends to thawing  
660 permafrost.

661 Although climate reanalysis and satellite gravimetry are too coarse to resolve  $<0.1 \text{ cm a}^{-1}$   
662 trends in active layer storage, the decisively positive ( $P - E - R$ ) supports an interpretation that  
663 the active layer was effectively saturated throughout the studied period. One consequence is that  
664 (34) and (35) cannot be expected to provide meaningful estimates of catchment-effective thaw  
665 rate, which was already unlikely given their simplification of active layer and the scale mismatch  
666 between reanalysis, GRACE, and  $\sim 8400 \text{ km}^2$  Kuparuk River basin. However, it also suggests the  
667 active groundwater layer thickness likely increased in proportion to the actual active layer  
668 thickness, and that predicted trends are candidate proxies for actual trends. If ( $P - E - R$ ) were  
669 decisively negative, predicted trends in active groundwater layer thickness would likely  
670 under-predict actual active layer trends owing to loss of storage to  $E + R$  (Brutsaert & Hiyama,  
671 2012). Climate reanalysis and satellite gravimetry may therefore prove useful for interpreting  
672 recession analysis predictions at broad scales and in regions without ground-based observations.

## 673 **6.2 Limitations of the method and suggestions for future research**

674 Section 3 presents a dramatic simplification of active layer hydrology, and we discuss a  
675 few salient criticisms. First, (1) acquires physical meaning from solutions to (4) that assume  
676 instantaneous drawdown of an initially saturated Boussinesq aquifer discharging to a fully- or  
677 partially-penetrating channel (Brutsaert & Nieber, 1977; van de Giesen et al., 2005; Rupp &  
678 Selker, 2005). This implies negligible influence of precipitation, evaporation, channel routing,  
679 overland flow, unsaturated flow, deep groundwater flow, and anything else that affects recession.  
680 Rather than assume negligible evaporation, future work could incorporate frameworks that  
681 include evaporation in (3) (Szilagyi et al., 2007; Zecharias & Brutsaert, 1988b) into the  
682 derivation that leads to (20).

683 Transient recharge, unsaturated flow, and aquifer compressibility, the latter of which is  
684 particularly relevant to thawing permafrost (Liljedahl et al., 2016), are thought to mainly affect  
685 early-time recession (Liang et al., 2017). This suggests possible bias when estimating  $\phi$  from  
686 early-time solutions using (26)–(28), which is a critical uncertainty because  $\phi$  is a small number  
687 in the denominator of (20). The actual aquifer-contributing area may also be smaller than the  
688 basin area. If so, the value of  $A$  in (26)–(28) is biased high and  $\phi$  is biased low. This may explain

689 why  $\phi$  estimates obtained from the method of (26)–(28) appear systematically low compared  
 690 with field-scale estimates (c.f. Equation 15 of Brutsaert & Nieber, 1977). Deep groundwater flow  
 691 paths, which are indicated by isolated aufeis in the lower reaches of the Kuparuk (Huryn et al.,  
 692 2021), are expected to have a similar effect (Liang et al., 2017).

693 Precipitation was mitigated by censoring flows within a six-day window of recorded  
 694 rainfall if a streamflow response was detected, whereas most prior works detected rainfall from  
 695 the streamflow response alone (Brutsaert & Hiyama, 2012; Cheng et al., 2016; Dralle et al.,  
 696 2017; Evans et al., 2020; many others). Using rainfall measurements to censor flows resulted in  
 697 fewer detected recession events, as expected. However, it unexpectedly eliminated the smallest  
 698 detected baseflow values because rainfall is common during Oct–Nov when the lowest baseflows  
 699 occur in the studied area. This reduced  $\langle\tau\rangle$  because  $\tau$  is inversely proportional to  $Q$  for  $b > 1$ ,  
 700 and may have contributed to the falloff at  $\tau > \sim 100$  days (Figure 6). This is a specific example  
 701 of a general result that  $\langle\tau\rangle$  depends on the sample space of  $Q$ , and indicates a possible low bias in  
 702  $\langle\tau\rangle$  from under-sampling the lowest flows. The inferred magnitude  $\langle\tau\rangle \cong 25$  days is about  
 703 two-thirds the canonical value 45 days obtained from linear recession analysis, whereas  $\langle t\rangle \cong 36$   
 704 days is within the  $\pm 15$  day characteristic uncertainty (Brutsaert, 2008; Brutsaert & Sugita, 2008;  
 705 Cooper et al., 2018). A detailed study of  $\tau$  sensitivity to methodology is needed and would likely  
 706 benefit from numerical simulation in addition to empirical estimation (c.f., Rupp et al., 2009).

### 707 **6.3 Implications for recession analysis and hydrologic signatures**

708 In Section 3 we showed that the nonlinear drainage timescale  $\tau$  follows an unbounded  
 709 Pareto distribution and a method to fit the distribution that provides an unbiased estimate of  $b$  in  
 710 the event-scale recession equation  $-dQ/dt = aQ^b$ . This provides an alternative to ordinary  
 711 least-squares fitting to a bi-logarithmic plot of  $Q$  versus  $-dQ/dt$ . In addition to retaining  
 712 large-sample information, a key benefit of this method is the absence of parameter  $a$  in the fitting  
 713 procedure. When individual recession events are plotted on a traditional point cloud diagram,  
 714 events with similar slope  $b$  but different intercept  $a$  produce a characteristic offset (Biswal &  
 715 Kumar, 2014; Jachens et al., 2020; Zecharias & Brutsaert, 1988a). A linear fit to the point cloud  
 716 systematically underestimates  $b$ , in a manner analogous to the bias induced by least squares  
 717 fitting to bivariate data with errors present in the independent variable (York et al., 2004). A  
 718 remarkable by-product of the procedure developed here is shown in Figure 7, where the detected

719 sample of underlying power-law distributed recession flows (red circles) occupy exactly that  
 720 portion of the point cloud where expert judgment would expect, far from the upper envelope,  
 721 near the smallest values of  $-dQ/dt$  for given  $Q$  (Brutsaert & Nieber, 1977; Rupp & Selker,  
 722 2006a).

723 This procedure also revealed that the drainage timescale  $\tau$  is equal to the threshold  $\tau_0$   
 724 plus a timescale dictated by the degree of nonlinearity encoded in  $b$ :

$$725 \quad \langle \tau \rangle = \tau_0 + (b - 1)\langle t \rangle. \quad (36)$$

726 This way of writing (10) has important implications for the use of characteristic  
 727 timescales as quantitative metrics of streamflow ('hydrologic signatures') (McMillan, 2020). It  
 728 reveals that a threshold exists below which theoretical late-time power-law scaling of baseflow is  
 729 not realized. Because  $\langle \tau \rangle$  and  $\tau_0$  together determine  $\langle t \rangle$  (the average duration of baseflow), they  
 730 are directly linked to water availability. Thresholds dictating the onset of critical behavior are  
 731 thoroughly understood generally (Aschwanden, 2015), and in porous media (Hunt & Ewing,  
 732 2009), but appear underexplored within the literature linking baseflow recession to hydrologic  
 733 signatures (McMillan, 2020). At hillslope scales,  $\tau_0$  can be interpreted as a timescale  
 734 representing the critical transition from "intermediate" ( $2 < b < 3$ ) to "late-time" ( $1 \leq b < 2$ )  
 735 recession (van de Giesen et al., 2005; Rupp & Selker, 2006b). At catchment scales,  $\tau_0$  represents  
 736 a transition from disordered to ordered flow dictated by a combination of threshold-like  
 737 processes that remain poorly understood (Troch et al., 2009).

## 738 **7 Conclusions**

739 We developed a theoretical framework to predict the long-term average rate of change of  
 740 permafrost active layer thickness using principles of hydraulic groundwater theory and nonlinear  
 741 baseflow recession analysis. Our method requires measurements of streamflow recession and  
 742 catchment topography, and therefore has potential to complement or extend the spatial and  
 743 temporal coverage of direct active layer measurements where few or none exist. Relative to  
 744 earlier equations derived from linear reservoir theory, our nonlinear analysis (Section 3) predicts  
 745 active layer may increase, decrease, or remain constant, depending on catchment topographic  
 746 slope, saturated lateral hydraulic conductivity, and the degree of nonlinearity in the catchment  
 747 storage-discharge relationship (or lack thereof). Critically, this implies that no unique functional  
 748 relationship exists between active layer thickness change and streamflow change within the

749 context of baseflow recession analysis, and calls for further comparison with active layer  
750 thickness measurements before the method is applied broadly.

751         A first application of our method to 38 years of daily streamflow observations in the  
752 Kuparuk River on the North Slope of Arctic Alaska suggests the active layer thickened by ~4.4  
753 cm between 1983–2020 and by ~6.2 cm between 1990–2020. Direct measurements of active  
754 layer thickness during the latter period indicate the active layer thickened at a rate ~55% higher  
755 than predicted. This suggests either the measurements overestimate the catchment-mean rate, or  
756 the baseflow prediction is too low. The predicted rate of change more than doubled between  
757 2002–2020, this time in closer agreement (+5%) with the observed rate. The inferred increase in  
758 subsurface water storage was corroborated by satellite gravimetry and climate reanalysis, which  
759 both indicate terrestrial water storage increased at rates that outpaced increases in subsurface  
760 water storage as the active layer thickened in response to permafrost thaw.

761         Overall, these findings suggest that both increased precipitation and permafrost thaw are  
762 playing increasingly important roles in sustaining baseflow in the Kuparuk River basin, and point  
763 to a growing importance of subsurface hydrologic processes in the region. Nonlinear baseflow  
764 recession analysis has potential to provide novel insight into these processes at the scale of river  
765 basins, and we provide a consistent analytical framework to explore them.

766 **Glossary**

$a, b$	General discharge recession constants.
$a_1, b_1$	Early-time discharge recession constants.
$a_2, b_2$	Late-time discharge recession constants.
$A$	Horizontal aquifer area, equal to $2LB$ .
$ALT$	Active layer thickness.
$B$	Aquifer breadth (distance along land surface).
$c_1, c_2$	Generic constant coefficients.
$D$	Aquifer thickness.
$E$	Evaporation per unit time.
$h$	Water table thickness.
$h_0$	Water table thickness at channel seepage face.
$I$	Recharge per unit time.
$K$	Aquifer drainage timescale for linear reservoir model.
$k$	Saturated lateral hydraulic conductivity.
$k_D$	Saturated lateral hydraulic conductivity at top of aquifer (entire aquifer if $k$ is constant).
$L$	Channel or stream length.
$n$	Exponent of hydraulic conductivity power-function.
$N$	Exponent of discharge recession constant $a$ power-function.
$P$	Precipitation per unit time.
$q$	Aquifer discharge per unit width of aquifer.
$Q$	Aquifer discharge, assumed equal to $2qL$ ; measured discharge assumed to be baseflow.
$Q_0$	Threshold aquifer discharge at onset of late-time recession.
$\bar{Q}$	Average aquifer discharge, assumed to equal average value of baseflow for timescales $>1$ year.
$R$	Runoff per unit time.
$S$	Aquifer storage.
$\bar{S}$	Average aquifer storage.
$S_c$	Critical aquifer storage at which discharge $Q$ equals $Q_{\min}$ .
$S_r$	Reference aquifer storage (arbitrary datum).
$T$	Thaw per unit time.
$t$	Time.
$x$	Horizontal coordinate.
$z$	Vertical coordinate.
$\alpha$	Exponent of Pareto distribution.
$\beta$	Exponent of storage-discharge function.
$\varepsilon$	Uncertainty interval half-width (error-margin).
$\zeta$	Exponent of generalized Pareto distribution.
$\lambda$	Sensitivity coefficient, equal to $\tau/\phi[1/(N + 1)]$ .
$\eta$	Average water table thickness during aquifer drawdown.
$\bar{\eta}$	Average water table thickness.
$\phi$	Drainable porosity.
$\theta$	Aquifer slope above horizontal base.
$\sigma$	Scale parameter of generalized Pareto distribution.
$\tau$	Aquifer drainage timescale for nonlinear reservoir model.
$\tau_0$	Threshold aquifer drainage timescale at onset of late-time recession.
$\tau_r$	Reference aquifer drainage timescale for nonlinear reservoir model.
$\mu$	Threshold parameter of generalized Pareto distribution.
$\langle \rangle$	Expected value of probability distribution.
$\hat{\phantom{x}}$	Parameter estimate.

768

769 **Appendix A**770 **A1 Particular solutions to the 1-D lateral groundwater flow equation**771 **A1.1 Horizontal aquifers**

772 Here we write particular forms of (20) and (22) based on late-time solutions to the 1-D  
 773 lateral flow equation for horizontal (hereafter ‘flat’) aquifers (Boussinesq, 1903, 1904; Rupp &  
 774 Selker, 2005). In doing so, we recover the earlier linear forms of (20) and (22) given in Brutsaert  
 775 and Hiyama (2012). It is helpful to first recapitulate that the parameters  $a$  and  $b$  can be  
 776 interpreted as solutions to the 1-D lateral flow equation for both flat and sloped aquifers:

$$777 \quad \frac{\partial h}{\partial t} = \frac{k}{\phi} \frac{\partial}{\partial x} \left[ h \left( \frac{\partial h}{\partial x} \cos \theta + \sin \theta \right) \right] + \frac{I}{\phi}, \quad (A1)$$

778 where  $h(x, t)$  is the phreatic water surface along dimension  $x$ ,  $k$  is lateral saturated hydraulic  
 779 conductivity,  $\theta$  is bed slope, and  $I$  is recharge rate.

780 Detailed descriptions of (A1) are widely available (e.g., Daly & Porporato, 2004); for our  
 781 purposes, we note a particular form of (A1) relevant to this analysis obtained by allowing  $k$  to  
 782 vary as a power function of distance along the dimension  $z$  perpendicular to the impermeable  
 783 base (Beven, 1982; Rupp & Selker, 2006b):

$$784 \quad \frac{\partial h}{\partial t} = \frac{k_D}{\phi} \frac{D^{-n}}{(n+1)} \frac{\partial}{\partial x} \left[ h^{n+1} \left( \frac{\partial h}{\partial x} \cos \theta + \sin \theta \right) \right] + \frac{I}{\phi} \quad (A2)$$

785 where:

$$786 \quad k(z) = k_D (z/D)^n, \quad (A3)$$

787 is the vertical variation in lateral saturated hydraulic conductivity,  $n$  is a constant, and  $k_D =$   
 788  $k(D)$  (the valid domain of  $n$  is discussed in Section 4.2). Solutions to (A1) and (A3) take the  
 789 form  $h(x, t)$  and are expressed (via integration) as discharge flux at the downslope channel per  
 790 unit width of aquifer:  $q(t) = f(a, b, q_0)$ , where  $q_0$  is discharge at the onset of recession and  
 791 catchment outlet discharge is  $Q(t) = 2qL$  where  $L$  is the length of all upstream channels. Head at  
 792 the downslope channel is  $h_0$ .

793 Two families of solutions to (A1)–(A3) are considered (Table A1), one for flat aquifers  
 794 (Rupp & Selker, 2005) and one for sloped aquifers (Rupp & Selker, 2006b) (hereafter RS05 and  
 795 RS06). Exact solutions have been obtained for  $h_0 = 0$  and approximations for  $0 < h_0 \leq D$ . As  
 796 mentioned in Section 3, we use the collated solutions in Figure 2 and Figure 3 from RS06 as the  
 797 basis for our generalization, and express (3) in terms of (17) for the case  $c_2 = 0$ . Beginning with  
 798 the flat-aquifer late-time analytical solution to (A2) from RS05:

$$799 \quad -\frac{dQ}{dt} = (c_1 D^{-\frac{n}{n+2}}) Q^{\frac{2n+3}{n+2}}, \quad (\text{A4})$$

800 we write this as:

$$801 \quad -\frac{dQ}{dt} = c_1 D^N Q^b, \quad (\text{A5})$$

802 which implies  $N = 3 - 2b$ , and:

$$803 \quad \frac{d\bar{\eta}}{dt} = \frac{\tau}{\phi} \left( \frac{1}{4 - 2b} \right) \frac{d\bar{Q}}{dt}. \quad (\text{A6})$$

804 This equation can be regarded as a general solution to (20), just as (A4) can be regarded  
 805 as a general solution to (A2), in the sense that any value of  $1 < b < 2$  obtained from recession  
 806 analysis can be interpreted in terms of  $n$  via (A3). This does not imply all values of  $b$  have a  
 807 physically meaningful interpretation (Section 4.2).

808 We now ask if (A5)–(A6) generalize to flat-aquifer solutions having a constant  $k(z)$   
 809 profile, as suggested in Section 3 via (17)–(18). Although this question can be answered by  
 810 simple inspection of  $a(D)$  for each of the six early-time solutions and noting that  $N = 3 - 2b$   
 811 holds in each case, stepping through them provides an opportunity to express (20) in terms of  
 812 (A6) for each particular value of  $b$ , and is useful when we move to the sloped-aquifer case. For  
 813 constant  $k(z)$ ,  $n = 0$ , which implies  $b = 3/2$ , which (as derived in RS05) is consistent with the  
 814 known nonlinear late-time exact solution for flat, homogeneous aquifers (Boussinesq, 1904). For  
 815 that solution,  $a \neq f(D)$ , meaning  $N = 0$ , and (A6) evaluates to:

$$816 \quad \frac{d\bar{\eta}}{dt} = \frac{\tau}{\phi} \frac{d\bar{Q}}{dt} \quad (\text{A7})$$

817 which is consistent with (18) for  $\partial_D a = 0$  and with (A6) for  $N = 3 - 2b$ , given  $b = 3/2$ .  
 818 Applied to the linearized late-time solution for homogeneous flat aquifers (Boussinesq, 1903),  
 819 we have  $b = 1$ ,  $N = 1$ , and:

$$820 \quad \frac{d\bar{\eta}}{dt} = \frac{\tau}{2\phi} \frac{d\bar{Q}}{dt} \quad (\text{A8})$$

821 which is consistent with (18) for  $\partial_D a = a/D$  and with (A6) for  $N = 3 - 2b$ , given  $b = 1$ .  
 822 Equation (A8) recovers Equation 10 of Brutsaert and Hiyama (2012), also derived from the  
 823 Boussinesq (1903) linearized solution. A similar substitution of  $N = 1$  into (22) recovers  
 824 Equation 13 of Brutsaert and Hiyama (2012), which can be expressed in terms of  $b$  for  $N = 3 -$   
 825  $2b$  as:

$$826 \quad \frac{d\bar{\eta}}{dt} = \frac{\eta}{a} \left( \frac{1}{3 - 2b} \right) \frac{da}{dt}. \quad (\text{A9})$$

827 Although our interest is in late-time solutions, a similar exercise verifies that (A4)–(A6)  
 828 are internally consistent for the three known early-time ( $b = 3$ ) solutions, one of which is exact,  
 829 but assumes  $h_0 = 0$  and infinite aquifer width (Polubarinova-Kochina, 1962). Specifically, if  
 830  $b = 3$ , then  $N = -3$ , and (A6) evaluates to  $d\bar{\eta}/dt = -(2\tau/\phi)d\bar{Q}/dt$ . This does not prove, but  
 831 rather demonstrates, as described in Section 3, via (16)–(20), that the definition  $b = (2n +$   
 832  $3)/(n + 2)$  and its relationship to  $a(D)$  via  $N = 3 - 2b$  generalizes the Brutsaert and Hiyama  
 833  $d\bar{\eta} \sim d\bar{Q}$  analysis to all known functional forms for flat aquifers, or those that can be considered  
 834 effectively flat.

Table 1: Late-time solutions and parameter definitions in  $-\frac{dQ}{dt} = c_1 D^N Q^b$  and  $\frac{d\bar{\eta}}{dt} = \frac{\bar{\tau}}{f} \left( \frac{1}{N+1} \right) \frac{d\bar{Q}}{dt}$

Form of Boussinesq equation	$b$	$N$ ( $= n(2-b)$ )	$\frac{\bar{\tau}}{f} \left( \frac{1}{N+1} \right)$	Downstream boundary condition	Reference
linearized	1	$3-2b$	$\frac{\tau}{2f}$	$h_0 = D$	Boussinesq, 1903
non-linear	$3/2$	$3-2b$	$\frac{\tau}{f}$	$h_0 = 0$	Boussinesq, 1904
non-linear	$\frac{2n+3}{n+2}$	$3-2b$	$\frac{\tau}{2f(2-b)}$	$h_0 = 0$	Rupp & Selker, 2005
linearized	1	$3-2b$	$\frac{\tau}{f}$	$h_0 = D$	Zecharias & Brutsaert, 1988
linearized	1	$3-2b$	$\frac{\tau}{f}$	$h_0 = D$	Sanford, 1993
linearized	1	$3-2b$	$\frac{\tau}{f}$	$h_0 = D$	Sanford, 1993
linearized	1	$3-2b$	$\frac{\tau}{f}$	$h_0 = D$	Steenhuis, 1999
linearized	1	$3-2b$	$\frac{\tau}{f}$	$h_0 = D$	Brutsaert, 1994
non-linear	$\frac{2n+1}{n+1}$	$1-b$	$\frac{\tau}{f(2-b)}$	$h_0 = D$	Rupp & Selker, 2006

835

## 836 **A1.2 Sloped aquifers**

837 We first note that a wider variety of solutions exist for sloped aquifers, all of which rely  
 838 on linearizations of (A2) and assumptions beyond our scope to thoroughly evaluate. As in the  
 839 previous section, we start with the general solution from RS06 for the  $k(z)$  profile given by  
 840 (A3), in this case for a sloped aquifer:

$$841 \quad -\frac{dQ}{dt} = (c_1 D^{-\frac{n}{n+1}}) Q^{\frac{2n+1}{n+1}} \quad (A10)$$

842 which, using the notation  $-dQ/dt = c_1 D^N Q^b$ , implies  $N = 1 - b$  and therefore:

$$843 \quad \frac{d\bar{\eta}}{dt} = \frac{\tau}{\phi} \left( \frac{1}{2-b} \right) \frac{d\bar{Q}}{dt}, \quad (A11)$$

844 which departs from (A6) by a factor of two.

845         As before, we now ask if (A10)–(A11) can be generalized to sloped-aquifer solutions  
846 with a constant  $k(z)$  profile. Setting aside kinematic wave solutions (e.g., Beven, 1982), six of  
847 the 11 sloped-aquifer solutions collated in Figure 3 of RS06 effectively treat  $a(D)$  as the  
848 horizontal equivalent multiplied by a dimensionless slope factor:  $\nu = B/D \tan \theta$ . Note that  $\nu$   
849 represents the balance of gravity-driven flow via  $\tan \theta$  versus diffusion via  $B/D$ .

850         In these cases, if  $\nu$  is treated as a constant parameter, all linearized sloped-aquifer  
851 solutions to (A2) conform to  $N = 3 - 2b$  and therefore (A6), along with two solutions for which  
852  $\nu$  is effectively zero. The remaining three solutions include (A10) and two based on (A10),  
853 which conform to  $N = 1 - b$  and therefore (A11). If  $\nu$  is not assumed constant, then (18) holds  
854 in some cases. Two examples are the late-time  $b = 1$  solution of Sanford et al. (1993) and the  
855 early-time  $b = 3$  solution of Brutsaert (1994) (Table A1).

856         Equation (A6) and Equation (A11) suggests two families of solutions are applicable. One  
857 solution family can be applied to flat (or effectively flat) aquifers, including those with a  $k(z)$   
858 profile described by (A3), and to linearized approximations for sloped aquifers with a constant  
859  $k(z)$  profile. For these solutions,  $N = 3 - 2b$  leads to (A6). The second solution family applies  
860 to sloped aquifers with a  $k(z)$  profile described by (A3), for which  $N = 1 - b$  leads to (A11).

861 **Acknowledgments**

862           The Interdisciplinary Research for Arctic Coastal Environments project funded this work  
863 through the United States Department of Energy, Office of Science, Biological and  
864 Environmental Research (BER) Regional and Global Model Analysis (RGMA) program areas,  
865 under contract grant #89233218CNA000001 to Triad National Security, LLC (“Triad”). The  
866 authors have no competing interests, financial or otherwise. Author contributions: MGC  
867 designed the study, performed the analysis, prepared the figures, and wrote the manuscript. TZ  
868 supervised the project. JCR oversaw funding and project supervision. JS, WRB, and KEB  
869 contributed to data curation. All authors contributed to research questions and edited the  
870 manuscript.

871

872 **Data and Software Availability**

873 Data and code required to reproduce all figures in this manuscript are available without  
874 restriction from <https://github.com/mgcooper/BFRA> (Cooper, 2022). The baseflow recession  
875 analysis algorithm (v1) is preserved and available without restriction from  
876 <https://github.com/mgcooper/BFRA>. Kuparuk River discharge data are archived at the USGS  
877 Water Data for the Nation (<https://waterdata.usgs.gov/monitoring-location/15896000/>). Rainfall  
878 data are archived at the United States National Centers for Environmental Information  
879 (<https://www.ncdc.noaa.gov/cdo-web/datasets/GHCND/stations/GHCND:USC00505136/detail>).  
880 MERRA2 climate reanalysis data are archived at the NASA Goddard Earth Sciences and Data  
881 Information Services Center (<https://disc.gsfc.nasa.gov/datasets?project=MERRA-2>). GRACE  
882 and GRACE-FO data are archived at the University of Texas at Austin Center for Space  
883 Research (<http://www2.csr.utexas.edu/grace>). Active layer thickness data provided by the  
884 Circumpolar Active Layer Monitoring program and the International Permafrost Association are  
885 archived at the Arctic Data Center (<https://arcticdata.io/catalog/portals/CALM>).

886

887 **References**

- 888 Aksoy, H., & Wittenberg, H. (2011). Nonlinear baseflow recession analysis in watersheds with intermittent  
889 streamflow. *Hydrological Sciences Journal*, *56*(2), 226–237.  
890 <https://doi.org/10.1080/02626667.2011.553614>
- 891 Arp, C. D., Whitman, M. S., Kemnitz, R., & Stuefer, S. L. (2020). Evidence of Hydrological Intensification and  
892 Regime Change From Northern Alaskan Watershed Runoff. *Geophysical Research Letters*, *47*(17),  
893 e2020GL089186. <https://doi.org/10.1029/2020GL089186>
- 894 Aschwanden, M. J. (2015). THRESHOLDED POWER LAW SIZE DISTRIBUTIONS OF INSTABILITIES IN  
895 ASTROPHYSICS. *The Astrophysical Journal*, *814*(1), 19. <https://doi.org/10.1088/0004-637X/814/1/19>
- 896 Berghuijs, W. R., Hartmann, A., & Woods, R. A. (2016). Streamflow sensitivity to water storage changes across  
897 Europe. *Geophysical Research Letters*, *43*(5), 1980–1987. <https://doi.org/10.1002/2016GL067927>
- 898 Beven, K. (1982). On subsurface stormflow: Predictions with simple kinematic theory for saturated and unsaturated  
899 flows. *Water Resources Research*, *18*(6), 1627–1633. <https://doi.org/10.1029/WR018i006p01627>
- 900 Biswal, B., & Kumar, D. N. (2014). Study of dynamic behaviour of recession curves. *Hydrological Processes*,  
901 *28*(3), 784–792. <https://doi.org/10.1002/hyp.9604>
- 902 Boussinesq, J. (1903). Sur le débit, en temps de sécheresse, d'une source alimentée par une nappe d'eaux  
903 d'infiltration. *CR Hebd. Seanc. Acad. Sci. Paris*, *136*, 1511–1517.
- 904 Boussinesq, J. (1904). Recherches théoriques sur l'écoulement des nappes d'eau infiltrées dans le sol et sur le débit  
905 des sources. *Journal de Mathématiques Pures et Appliquées*, *10*, 5–78.
- 906 Brutsaert, W. (1994). The unit response of groundwater outflow from a hillslope. *Water Resources Research*,  
907 *30*(10), 2759–2763. <https://doi.org/10.1029/94WR01396>
- 908 Brutsaert, W. (2005). *Hydrology: An Introduction*. Cambridge: Cambridge University Press.  
909 <https://doi.org/10.1017/CBO9780511808470>
- 910 Brutsaert, W. (2008). Long-term groundwater storage trends estimated from streamflow records: Climatic  
911 perspective. *Water Resources Research*, *44*(2), W02409. <https://doi.org/10.1029/2007WR006518>
- 912 Brutsaert, W., & Hiyama, T. (2012). The determination of permafrost thawing trends from long-term streamflow  
913 measurements with an application in eastern Siberia. *Journal of Geophysical Research: Atmospheres*,  
914 *117*(D22). <https://doi.org/10.1029/2012JD018344>
- 915 Brutsaert, W., & Nieber, J. L. (1977). Regionalized drought flow hydrographs from a mature glaciated plateau.  
916 *Water Resources Research*, *13*(3), 637–643. <https://doi.org/10.1029/WR013i003p00637>
- 917 Brutsaert, W., & Sugita, M. (2008). Is Mongolia's groundwater increasing or decreasing? The case of the Kherlen  
918 River basin / Les eaux souterraines de Mongolie s'accroissent ou décroissent-elles? Cas du bassin versant  
919 la Rivière Kherlen. *Hydrological Sciences Journal*, *53*(6), 1221–1229.  
920 <https://doi.org/10.1623/hysj.53.6.1221>
- 921 Cheng, L., Zhang, L., & Brutsaert, W. (2016). Automated Selection of Pure Base Flows from Regular Daily  
922 Streamflow Data: Objective Algorithm. *Journal of Hydrologic Engineering*, *21*(11), 06016008.  
923 [https://doi.org/10.1061/\(ASCE\)HE.1943-5584.0001427](https://doi.org/10.1061/(ASCE)HE.1943-5584.0001427)
- 924 Clauset, A., Shalizi, C. R., & Newman, M. E. J. (2009). Power-Law Distributions in Empirical Data. *SIAM Review*,  
925 *51*(4), 661–703. <https://doi.org/10.1137/070710111>
- 926 Cooper, M. G. (2022). Baseflow recession analysis (BFRA) (Version 1). Richland, WA: Pacific Northwest National  
927 Laboratory. Retrieved from <https://github.com/mgcooper/BFRA>
- 928 Cooper, M. G., Schaperow, J. R., Cooley, S. W., Alam, S., Smith, L. C., & Lettenmaier, D. P. (2018). Climate  
929 Elasticity of Low Flows in the Maritime Western U.S. Mountains. *Water Resources Research*, *54*(8), 5602–  
930 5619. <https://doi.org/10.1029/2018WR022816>
- 931 Daly, E., & Porporato, A. (2004). A note on groundwater flow along a hillslope. *Water Resources Research*, *40*(1).  
932 <https://doi.org/10.1029/2003WR002438>

- 933 Dralle, D. N., Karst, N. J., Charalampous, K., Veenstra, A., & Thompson, S. E. (2017). Event-scale power law  
 934 recession analysis: quantifying methodological uncertainty. *Hydrology and Earth System Sciences*, 21(1),  
 935 65–81. <https://doi.org/10.5194/hess-21-65-2017>
- 936 Duan, L., Man, X., Kurylyk, B. L., & Cai, T. (2017). Increasing Winter Baseflow in Response to Permafrost Thaw  
 937 and Precipitation Regime Shifts in Northeastern China. *Water*, 9(1). <https://doi.org/10.3390/w9010025>
- 938 Earth Resources Observation And Science (EROS) Center. (2018). Interferometric Synthetic Aperture Radar  
 939 (IFSAR) Alaska [Data set]. U.S. Geological Survey. <https://doi.org/10.5066/P9C064CO>
- 940 Evans, S. G., Yokeley, B., Stephens, C., & Brewer, B. (2020). Potential mechanistic causes of increased baseflow  
 941 across northern Eurasia catchments underlain by permafrost. *Hydrological Processes*, 34(11), 2676–2690.  
 942 <https://doi.org/10.1002/hyp.13759>
- 943 Feng, D., Gleason, C. J., Lin, P., Yang, X., Pan, M., & Ishitsuka, Y. (2021). Recent changes to Arctic river  
 944 discharge. *Nature Communications*, 12(1), 6917. <https://doi.org/10.1038/s41467-021-27228-1>
- 945 GDAL/OGR contributors. (2022). *GDAL/OGR Geospatial Data Abstraction software Library*. Open Source  
 946 Geospatial Foundation. <https://doi.org/10.5281/zenodo.5884351>
- 947 Gelaro, R., McCarty, W., Suárez, M. J., Todling, R., Molod, A., Takacs, L., et al. (2017). The Modern-Era  
 948 Retrospective Analysis for Research and Applications, Version 2 (MERRA-2). *Journal of Climate*, 30(14),  
 949 5419–5454. <https://doi.org/10.1175/JCLI-D-16-0758.1>
- 950 van de Giesen, N., Steenhuis, T. S., & Parlange, J.-Y. (2005). Short- and long-time behavior of aquifer drainage  
 951 after slow and sudden recharge according to the linearized Laplace equation. *Advances in Water Resources*,  
 952 28(10), 1122–1132. <https://doi.org/10.1016/j.advwatres.2004.12.002>
- 953 Hanel, R., Corominas-Murtra, B., Liu, B., & Thurner, S. (2017). Fitting power-laws in empirical data with  
 954 estimators that work for all exponents. *PLOS ONE*, 12(2), e0170920.  
 955 <https://doi.org/10.1371/journal.pone.0170920>
- 956 Hinzman, A. M., Sjöberg, Y., Lyon, S. W., Ploum, S. W., & van der Velde, Y. (2020). Increasing non-linearity of  
 957 the storage-discharge relationship in sub-Arctic catchments. *Hydrological Processes*, 34(19), 3894–3909.  
 958 <https://doi.org/10.1002/hyp.13860>
- 959 Hunt, A. G., & Ewing, R. P. (2009). *Percolation theory for flow in porous media* (2nd ed). Berlin: Springer.
- 960 Hury, A. D., Gooseff, M. N., Hendrickson, P. J., Briggs, M. A., Tape, K. D., & Terry, N. C. (2021). Aufeis fields  
 961 as novel groundwater-dependent ecosystems in the arctic cryosphere. *Limnology and Oceanography*, 66(3),  
 962 607–624. <https://doi.org/10.1002/lno.11626>
- 963 Jachens, E. R., Rupp, D. E., Roques, C., & Selker, J. S. (2020). Recession analysis revisited: impacts of climate on  
 964 parameter estimation. *Hydrol. Earth Syst. Sci.*, 24(3), 1159–1170. <https://doi.org/10.5194/hess-24-1159-2020>
- 966 Jacques, J.-M. S., & Sauchyn, D. J. (2009). Increasing winter baseflow and mean annual streamflow from possible  
 967 permafrost thawing in the Northwest Territories, Canada. *Geophysical Research Letters*, 36(1).  
 968 <https://doi.org/10.1029/2008GL035822>
- 969 Kane, D., Hinzman, L., Stuefer, S., & Arp, C. (2021). Updated Meteorological, Radiation, and Soil Temperature  
 970 Data, Kuparuk River and Nearby Watersheds: Imnavait B site (IB), 1986-2018. [Text/xml]. NSF Arctic  
 971 Data Center. <https://doi.org/10.18739/A2TQ5RF72>
- 972 Kirchner, J. W. (2009). Catchments as simple dynamical systems: Catchment characterization, rainfall-runoff  
 973 modeling, and doing hydrology backward. *Water Resources Research*, 45(2).  
 974 <https://doi.org/10.1029/2008WR006912>
- 975 Kurylyk, B. L., MacQuarrie, K. T. B., & McKenzie, J. M. (2014). Climate change impacts on groundwater and soil  
 976 temperatures in cold and temperate regions: Implications, mathematical theory, and emerging simulation  
 977 tools. *Earth-Science Reviews*, 138, 313–334. <https://doi.org/10.1016/j.earscirev.2014.06.006>

- 978 Liang, X., Zhan, H., Zhang, Y.-K., & Schilling, K. (2017). Base flow recession from unsaturated-saturated porous  
979 media considering lateral unsaturated discharge and aquifer compressibility. *Water Resources Research*,  
980 53(9), 7832–7852. <https://doi.org/10.1002/2017WR020938>
- 981 Liljedahl, A. K., Boike, J., Daanen, R. P., Fedorov, A. N., Frost, G. V., Grosse, G., et al. (2016). Pan-Arctic ice-  
982 wedge degradation in warming permafrost and its influence on tundra hydrology. *Nature Geoscience*, 9(4),  
983 312–318. <https://doi.org/10.1038/ngeo2674>
- 984 Luo, D., Wu, Q., Jin, H., Marchenko, S. S., Lü, L., & Gao, S. (2016). Recent changes in the active layer thickness  
985 across the northern hemisphere. *Environmental Earth Sciences*, 75(7), 555. [https://doi.org/10.1007/s12665-](https://doi.org/10.1007/s12665-015-5229-2)  
986 015-5229-2
- 987 Lv, M., Xu, Z., Yang, Z.-L., Lu, H., & Lv, M. (2021). A Comprehensive Review of Specific Yield in Land Surface  
988 and Groundwater Studies. *Journal of Advances in Modeling Earth Systems*, 13(2), e2020MS002270.  
989 <https://doi.org/10.1029/2020MS002270>
- 990 Lyon, S. W., & Destouni, G. (2010). Changes in Catchment-Scale Recession Flow Properties in Response to  
991 Permafrost Thawing in the Yukon River Basin. *International Journal of Climatology*, 30(14), 2138–2145.  
992 <https://doi.org/10.1002/joc.1993>
- 993 Lyon, S. W., Destouni, G., Giesler, R., Humborg, C., Mörth, M., Seibert, J., et al. (2009). Estimation of permafrost  
994 thawing rates in a sub-arctic catchment using recession flow analysis. *Hydrol. Earth Syst. Sci.*, 13(5), 595–  
995 604. <https://doi.org/10.5194/hess-13-595-2009>
- 996 McKenzie, J. M., Kurylyk, B. L., Walvoord, M. A., Bense, V. F., Fortier, D., Spence, C., & Grenier, C. (2021).  
997 Invited perspective: What lies beneath a changing Arctic? *The Cryosphere*, 15(1), 479–484.  
998 <https://doi.org/10.5194/tc-15-479-2021>
- 999 McMillan, H. (2020). Linking hydrologic signatures to hydrologic processes: A review. *Hydrological Processes*,  
1000 34(6), 1393–1409. <https://doi.org/10.1002/hyp.13632>
- 1001 McNamara, J. P., Kane, D. L., & Hinzman, L. D. (1998). An analysis of streamflow hydrology in the Kuparuk River  
1002 Basin, Arctic Alaska: a nested watershed approach. *Journal of Hydrology*, 206(1), 39–57.  
1003 [https://doi.org/10.1016/S0022-1694\(98\)00083-3](https://doi.org/10.1016/S0022-1694(98)00083-3)
- 1004 Nyland, K. E., Shiklomanov, N. I., Streletskiy, D. A., Nelson, F. E., Klene, A. E., & Kholodov, A. L. (2021). Long-  
1005 term Circumpolar Active Layer Monitoring (CALM) program observations in Northern Alaskan tundra.  
1006 *Polar Geography*, 44(3), 167–185. <https://doi.org/10.1080/1088937X.2021.1988000>
- 1007 O'Connor, M. T., Cardenas, M. B., Neilson, B. T., Nicholaides, K. D., & Kling, G. W. (2019). Active Layer  
1008 Groundwater Flow: The Interrelated Effects of Stratigraphy, Thaw, and Topography. *Water Resources*  
1009 *Research*, 55(8), 6555–6576. <https://doi.org/10.1029/2018WR024636>
- 1010 Polubarinova-Kochina, P. I. (1962). *Theory of ground water movement*. Princeton, N.J.: Princeton University Press.
- 1011 Rantz, S. E. (1982). *Measurement and computation of streamflow: Volume 1. Measurement of Stage and Discharge*  
1012 (USGS Numbered Series No. 2175). *Measurement and computation of streamflow* (Vol. 2175). U.S.  
1013 G.P.O. <https://doi.org/10.3133/wsp2175>
- 1014 Rawlins, M. A., Cai, L., Stuefer, S. L., & Nicolsky, D. (2019). Changing characteristics of runoff and freshwater  
1015 export from watersheds draining northern Alaska. *The Cryosphere*, 13(12), 3337–3352.  
1016 <https://doi.org/10.5194/tc-13-3337-2019>
- 1017 Rennermalm, A. K., Wood, E. F., & Troy, T. J. (2010). Observed changes in pan-arctic cold-season minimum  
1018 monthly river discharge. *Climate Dynamics*, 35(6), 923–939. <https://doi.org/10.1007/s00382-009-0730-5>
- 1019 Roques, C., Rupp, D. E., & Selker, J. S. (2017). Improved streamflow recession parameter estimation with attention  
1020 to calculation of  $-dQ/dt$ . *Advances in Water Resources*, 108, 29–43.  
1021 <https://doi.org/10.1016/j.advwatres.2017.07.013>
- 1022 Rowland, J. C., Travis, B. J., & Wilson, C. J. (2011). The role of advective heat transport in talik development  
1023 beneath lakes and ponds in discontinuous permafrost. *Geophysical Research Letters*, 38(17).  
1024 <https://doi.org/10.1029/2011GL048497>

- 1025 Rupp, D. E., & Selker, J. S. (2005). Drainage of a horizontal Boussinesq aquifer with a power law hydraulic  
1026 conductivity profile. *Water Resources Research*, 41(11), W11422. <https://doi.org/10.1029/2005WR004241>
- 1027 Rupp, D. E., & Selker, J. S. (2006a). Information, artifacts, and noise in  $dQ/dt - Q$  recession analysis. *Advances in*  
1028 *Water Resources*, 29(2), 154–160. <https://doi.org/10.1016/j.advwatres.2005.03.019>
- 1029 Rupp, D. E., & Selker, J. S. (2006b). On the use of the Boussinesq equation for interpreting recession hydrographs  
1030 from sloping aquifers. *Water Resources Research*, 42(12), W12421.  
1031 <https://doi.org/10.1029/2006WR005080>
- 1032 Rupp, D. E., Schmidt, J., Woods, R. A., & Bidwell, V. J. (2009). Analytical assessment and parameter estimation of  
1033 a low-dimensional groundwater model. *Journal of Hydrology*, 377(1–2), 143–154.  
1034 <https://doi.org/10.1016/j.jhydrol.2009.08.018>
- 1035 Sanford, W. E., Parlange, J.-Y., & Steenhuis, T. S. (1993). Hillslope drainage with sudden drawdown: Closed form  
1036 solution and laboratory experiments. *Water Resources Research*, 29(7), 2313–2321.  
1037 <https://doi.org/10.1029/93WR00515>
- 1038 Save, H., Bettadpur, S., & Tapley, B. D. (2016). High-resolution CSR GRACE RL05 mascons. *Journal of*  
1039 *Geophysical Research: Solid Earth*, 121(10), 7547–7569. <https://doi.org/10.1002/2016JB013007>
- 1040 Sergeant, F., Therrien, R., Oudin, L., Jost, A., & Anctil, F. (2021). Evolution of Arctic rivers recession flow: Global  
1041 assessment and data-based attribution analysis. *Journal of Hydrology*, 601, 126577.  
1042 <https://doi.org/10.1016/j.jhydrol.2021.126577>
- 1043 Sjöberg, Y., Jan, A., Painter, S. L., Coon, E. T., Carey, M. P., O'Donnell, J. A., & Koch, J. C. (2021). Permafrost  
1044 Promotes Shallow Groundwater Flow and Warmer Headwater Streams. *Water Resources Research*, 57(2),  
1045 e2020WR027463. <https://doi.org/10.1029/2020WR027463>
- 1046 Smith, L. C., Pavelsky, T. M., MacDonald, G. M., Shiklomanov, A. I., & Lammers, R. B. (2007). Rising minimum  
1047 daily flows in northern Eurasian rivers: A growing influence of groundwater in the high-latitude hydrologic  
1048 cycle. *Journal of Geophysical Research: Biogeosciences*, 112(G4). <https://doi.org/10.1029/2006JG000327>
- 1049 Szilagyi, J., Gribovszki, Z., & Kalicz, P. (2007). Estimation of catchment-scale evapotranspiration from baseflow  
1050 recession data: Numerical model and practical application results. *Journal of Hydrology*, 336(1), 206–217.  
1051 <https://doi.org/10.1016/j.jhydrol.2007.01.004>
- 1052 Taylor, B. N., & Kuyatt, C. E. (1994). *Guidelines for Evaluating and Expressing the Uncertainty of NIST*  
1053 *Measurement Results (NIST Technical Note vol 1297)* (p. 24). Gaithersburg, MD: National Institute of  
1054 Standards and Technology. Retrieved from <http://physics.nist.gov/Pubs/guidelines/TN1297/tm1297s.pdf>
- 1055 Troch, P. A., Carrillo, G. A., Heidbüchel, I., Rajagopal, S., Switanek, M., Volkmann, T. H. M., & Yaeger, M.  
1056 (2009). Dealing with Landscape Heterogeneity in Watershed Hydrology: A Review of Recent Progress  
1057 toward New Hydrological Theory. *Geography Compass*, 3(1), 375–392. <https://doi.org/10.1111/j.1749-8198.2008.00186.x>
- 1059 Tsallis, C. (1988). Possible generalization of Boltzmann-Gibbs statistics. *Journal of Statistical Physics*, 52(1), 479–  
1060 487. <https://doi.org/10.1007/BF01016429>
- 1061 Walvoord, M. A., & Kurylyk, B. L. (2016). Hydrologic Impacts of Thawing Permafrost-A Review. *Vadose Zone*  
1062 *Journal*, 15(6), vzj2016.01.0010. <https://doi.org/10.2136/vzj2016.01.0010>
- 1063 Walvoord, M. A., & Striegl, R. G. (2007). Increased groundwater to stream discharge from permafrost thawing in  
1064 the Yukon River basin: Potential impacts on lateral export of carbon and nitrogen. *Geophysical Research*  
1065 *Letters*, 34(12). <https://doi.org/10.1029/2007GL030216>
- 1066 Walvoord, M. A., Voss, C. I., & Wellman, T. P. (2012). Influence of permafrost distribution on groundwater flow in  
1067 the context of climate-driven permafrost thaw: Example from Yukon Flats Basin, Alaska, United States.  
1068 *Water Resources Research*, 48(7). <https://doi.org/10.1029/2011WR011595>
- 1069 Yang, D., Kane, D., Zhang, Z., Legates, D., & Goodison, B. (2005). Bias corrections of long-term (1973–2004)  
1070 daily precipitation data over the northern regions. *Geophysical Research Letters*, 32(19).  
1071 <https://doi.org/10.1029/2005GL024057>

- 1072 Yi, S., & Sneeuw, N. (2021). Filling the Data Gaps Within GRACE Missions Using Singular Spectrum Analysis.  
1073 *Journal of Geophysical Research: Solid Earth*, 126(5), e2020JB021227.  
1074 <https://doi.org/10.1029/2020JB021227>
- 1075 York, D., Evensen, N. M., Martínez, M. L., & De Basabe Delgado, J. (2004). Unified equations for the slope,  
1076 intercept, and standard errors of the best straight line. *American Journal of Physics*, 72(3), 367–375.  
1077 <https://doi.org/10.1119/1.1632486>
- 1078 Zecharias, Y. B., & Brutsaert, W. (1988a). Recession characteristics of groundwater outflow and base flow from  
1079 mountainous watersheds. *Water Resources Research*, 24(10), 1651–1658.  
1080 <https://doi.org/10.1029/WR024i010p01651>
- 1081 Zecharias, Y. B., & Brutsaert, W. (1988b). The influence of basin morphology on groundwater outflow. *Water*  
1082 *Resources Research*, 24(10), 1645–1650. <https://doi.org/10.1029/WR024i010p01645>
- 1083